Development of a Novel Technology for Rapidly Austenitizing Usibor® 1500P Steel

by

Joshua Rasera

A thesis
presented to the University of Waterloo
in fulfillment of the
thesis requirement for the degree of
Master of Applied Science
in
Mechanical Engineering

Waterloo, Ontario, Canada, Year

Author’s Declaration

I hereby declare that I am the sole author of this thesis. This is a true copy of the thesis, including any required final revisions, as accepted by my examiners.

I understand that my thesis may be made electronically available to the public.

Abstract

Hot forming die quenching (HFDQ) is a relatively new process in the field of automotive manufacturing. It involves slowly heating Usibor® 1500P steel (a 22MnB5 steel substrate with a protective Al-Si coating) sheets to temperatures exceeding 880 °C, and holding it for a fixed amount of time to ensure the crystallographic structure has become fully austenitic. Once austenitized, the steel is then simultaneously formed and quenched into complex geometries in a single stroke. The quenching stage is critical, allowing for the formation of a hard and strong martensitic crystal structure that would not otherwise be formable at room temperature. These high-strength steel members allow automotive manufacturers to use thinner material cross sections in structural members, thereby reducing the net vehicle weight and improving fuel efficiency without compromising crash performance.

Most HFDQ lines use roller hearth furnaces to austenitize ultra high strength steel blanks. While this process is a capable, proven industrial technology, it is limited to relatively inefficient modes of heat transfer, and thus requires long heating times, large furnaces, and considerable energy to maintain temperature. It is the purpose of this work to describe an alternative heating technology in which Usibor® 1500P coupons are austenitized by bringing them into contact with an electrically-heated monolith. In a laboratory-scale prototype, Usibor® coupons were austenitized in less than 25 seconds; subsequent material characterization and dilatometry investigations confirm that a fully martensitic structure is formed, and that the hardness and yield strength are comparable to furnace-treated samples.

Tailoring material properties in HFDQ structural members (body-in-white components) introduces a combination of strong martensitic structures and other softer, more ductile daughter phases such as bainite, ferrite, and pearlite. Most tailoring efforts have focused on controlling the localized quenching rate during the forming stage through selective heating and cooling of the forming dies. This work presents an alternative, based on direct contact heating, in which tailoring is achieved through non-uniform austenitization during the heating stage of HFDQ. Experiments carried out on Usibor® 1500P coupons show that it is possible to create a

fully-hardened zone within the coupon that transitions from martensite to softer phases over a relatively short distance.

Acknowledgements

I would like to begin by thanking my supervisor, Professor Kyle Daun, for his guidance and support over the past three years. His dedication to continuous engineering innovation in Canada and abroad is truly inspiring. He embodies what I believe it means to be a scientist, and I hope to one day be able to emulate his passion and work ethic in everything I do.

I would like to thank my industrial sponsor, F&P Manufacturing, Inc., for providing financial support and technical expertise on this project. In particular, I would like to single out Mike D'Souza, as his experience and constant enthusiasm for this project really helped to carry forward my work.

This work would not have been possible without the efforts of Eckhard Budziarek, Andy Barber, and Neil Griffett. Their knowledge and experience was immensely helpful to one, such as myself, who is rather hopeless at designing electrical circuits and control systems.

I would like to thank Professor Michael Worswick for generously allowing me to use his lab space for my experiments.

I would like to thank Brad Froese, Cameron Rush, and Peter Plaisier for their work on the initial design of this monolith for our Fourth Year Capstone Design Project. This die would never have exceeded room temperature without the three of you.

I would like to thank ArcelorMittal and Ron Soldaat for providing us with the Usibor® 1500P coupons that were used in our experiments, as well as for their willingness to aid us in any way possible.

I would like to thank my lab mates, both past and present, including Kamal Jhajj, Roger Tsang, Jeff Hou, Natalie Field, Sam Grauer, Tim Sipkens, Nigel Singh, Noel Chester, Paul Hadwin, Cangji Shi, and Etienne Caron for their friendship and support. You are all funny, intelligent, kind people, and it has truly been a privilege work with you and to call you friends.

I would like to thank my friends and roommates for putting up with my moodiness after long days spent on campus. You all have made the last few years incredibly awesome - I am very lucky to have such wonderful friends.

Lastly, I would like to thank my family. To Mum, Dad, Ben, and Gramma, thank you so much for endless love and support during both my M.A.Sc. and B.A.Sc. - I definitely would not have been able to get this far without you! To my late Grampa, Nonno and Nonna, you were all my champions from the day I was born, and I know that you still support me in everything I do in spirit; I wish you could all be here to celebrate this milestone with me. And finally, to Katie, you have been there for me on every good and bad day for the last 5 years, and you have been supportive of all of my goals and aspirations no matter how crazy and far out. Thank you so much for your love and support, and everything that you do for me – we make an amazing team!

For my family and for Katie.

Table of Contents

List of Figures

List of Tables

Chapter 1
Introduction

1.1 Motivation

Hot-forming-die-quenching (HFDQ) is used to form light-weight and high-strength structural automotive components, such as A-pillars, B-pillars, roof rails, and engine struts, out of ultrahigh strength steel (UHSS). In this process, sheet steel made from an alloy containing primarily manganese and a small amount of boron is cut into the desired 2D pattern known as a 'blank'. Blanks are then austenitized by heating them to approximately 950°C, usually within a roller hearth furnace. The blanks are then transferred to a chilled die, in which they are simultaneously formed and quenched. The advantage of HFDQ-formed UHSS parts is that they are able provide the same crash performance with a thinner material cross section compared to a cold-stamped part; thinner material allows for the net vehicle weight to be reduced, thereby allowing for improvements to fuel efficiency. Additionally, the high ductility and low flow stress of the hot UHSS blanks allows complex geometries to be formed with a single stroke.

While HFDQ is a relatively new-comer to the automotive manufacturing industry, many original equipment manufacturers (OEMs) and tier one supply companies are looking to adopt this technology to become more competitive in their industry. Despite the ubiquity of traditional roller hearth furnaces in hot stamping, they have a number of key drawbacks: the furnaces have high capital and operating costs, and require enormous amounts of floor space; the Al-Si protective coating tends to melt and impregnate the expensive ceramic rollers that convey the blanks, scoring the protective Al-Si-Fe layer and shortening the roller lifespan; and the molten Al-Si coating causes the coupons to slide on the ceramic rollers, complicating automated coupon transfer from the furnace to the press. Therefore, it is the purpose of this work to propose an alternative to the current industry standard for HFDQ: a novel process designed to utilize an in-line heated monolith to rapidly and efficiently transfer heat via conduction into room-temperature UHSS blanks. This direct-contact process, in turn, leads to greatly reduced energy consumption during manufacturing, thus allowing for savings to be

passed on to the consumer. Additionally, reduced material costs, and a more space- and time-efficient manufacturing process compared to the current state-of-the-art, allow for additional cost savings to be realized by the user as well.

Finally, there is presently an interest in academia and in industry to develop processes in which blanks are formed with an induced crystallographic gradient; segments containing strong and durable martensite alongside ones with more ductile daughter phases, such as bainite, ferrite, and pearlite, allow for improved crash performance of certain structural members. This work also explores how direct-contact heating can be applied to material property tailoring.

1.2 Industrial Context

The work presented in this thesis was done in collaboration with F&P Manufacturing Inc. (F&P), the Canadian subsidiary of F-Tech Inc. F&P is a tier one automotive manufacturing supplier located in Tottenham, Ontario, and presently do not possess hot-forming capabilities. In 2012, F&P approached the University of Waterloo looking to develop a research project exploring an alternative heating methodology to roller hearth furnaces. The ultimate goal of this collaboration is to develop and install a new heating technology in their facility that will offer them a process that allows them to produce hot formed parts within specification at a lower cost compared to their competitors.

1.3 Literature Review

Since its first adoption by the automotive industry in 1984, annual production of HFDQ parts has grown dramatically, estimated to have reached 450 million parts per year in 2013 [1]. In many modern vehicles, HFDQ is used to form a large proportion of structural members, as shown in Figure 1, and this number will only increase with further advances in this manufacturing technology. Given the rapid growth in hot stamping, and the competitiveness of the automotive industry, there is tremendous pressure to improve production efficiency by shortening the process cycle. International academic- and industry-based research efforts have focused mainly on shortening the stamping phase: Behrens et al. [2], Ingebrand et al. [3],

Gucker [4], and Lenze et al. [5] summarize some of the recent work in this area. Innovations to the heating phase, on the other hand, have been comparatively limited, as noted by Kolleck et al. [6] and Steinhoff et al. [7].

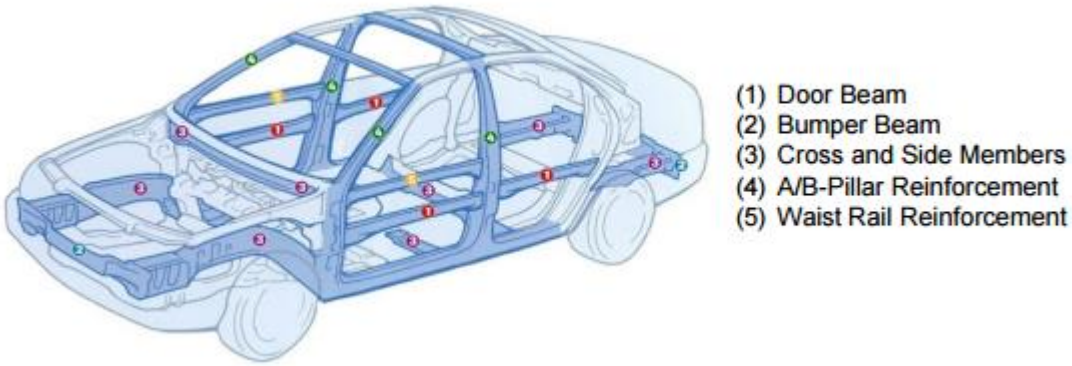

Figure 1 - HFDQ components currently being used or under development. Adapted from [8].

The majority of hot stamping lines use roller hearth furnaces, in which the coupons are conveyed through a sequence of zones that radiatively-heat the blanks according to a prescribed schedule. While recent research activities have attempted to address some of problems previously noted, such as the low profile batch furnaces analyzed by Twynstra et al. [9], and Lehmann's [10] work on new developments in ceramic roller coatings, these issues remain largely unresolved. These shortcomings have motivated development of alternative, non-radiative heating technologies, including: electrical resistance heating; induction heating; and direct contact heating. Novel heating technologies aim to improve cycle time, reduce energy consumption, and to develop customized surface coatings and material structures.

While the objective of most HFDQ lines is to obtain parts having uniform material properties, there is a growing interest in improving the crash performance through "tailoring," i.e. achieving engineered, non-uniform material properties in the formed parts. Most often, tailoring is done by uniformly heating the blank, and then controlling the local quenching rates by selectively heating and cooling the forming die [11]. Any regions quenched at rates greater than a critical rate (approximately 27 K/s) transform into martensite, while regions quenched

more slowly transform into more ductile daughter phases, such as bainite, ferrite, and pearlite [12]. It is the more ductile phases that are able to absorb more energy in a collision [13], whereas the martensitic allows for improved strength and reduced material thickness.

Tailored properties can also be obtained through non-uniform heating of the blanks, since regions whose local temperatures do not surpass the austenite start point will retain some, if not all, of the as-received material properties, whereas those regions that are sufficiently heated would be able to transform into martensite. This procedure requires localized, highly-controlled heating rates over the blank, which is very difficult to obtain in roller-hearth furnaces. Wilsius et al. [14] utilized heat shields installed with a furnace in order to selectively heat the blanks; they reported the tailored region possessing an ultimate tensile strength (UTS) of 700 MPa, and a UTS of 1600 MPa in the fully hardened region. Similarly, Stöhr et al. [15] performed patched heating experiments, and reported a tailored UTS of 1100 MPa, and the fully hardened region UTS of 1600 MPa.

1.4 Present Work

This work proposes a turnkey design process for a direct-contact heating monolith for HFDQ. Chapter 2 begins by providing insight to the advantages of HFDQ over common cold-forming, and discusses the unique material properties of the steel generally used in this process. Several state-of-the-art approaches that have been proposed in the literature for rapidly heating steel blanks, including traditional roller hearth furnaces, resistance heating, induction heating, and direct contact heating, are presented. The individual merits and drawbacks of each process are analyzed, and a recommendation is provided for the heating methodology to be developed. Additionally, this chapter presents current state-of-the-art methods used for tailoring the material properties within the steel blanks.

Chapter 3 builds upon the findings of Chapter 2, and discusses the design of a direct contact heating monolith, including material selection, heating methodology, and lab space considerations. The principles of heat transfer governing the operation of a direct contact heating monolith are presented alongside several numerical models used to predict how the monolith would function during testing for both homogeneously-heated and tailored coupons,

given the materials chosen. The mathematical formulations behind these models are also discussed.

Chapter 4 presents the proposed lab testing procedure, including a discussion of data collection methods and control systems used during testing. A discussion of the post-heat-treatment material testing methods used to analyze the properties of the treated steel and to validate the process is provided. A method for determining the extent of the austenitization of the coupons is also demonstrated.

Chapter 5 aims to present the results and a discussion of both the lab-scale testing and post-heat-treatment analysis. A holistic 'functional' analysis of the process is presented, as is a rigorous analysis of the data gathered during testing and from post-processing. This data is, in turn, used to validate the numerical models presented in Chapter 3, and to investigate the effects of rapid heating on the austenitization of the steel.

Chapter 6 builds upon the results reported in Chapter 5, and presents the development of a direct contact heating process designed to tailor the material properties of the heat treated coupon. Material selection, 1D and 3D modelling, adaptations to the basic experimental procedure, and experimental results are presented and discussed.

Finally, Chapter 7 summarizes the main conclusions of this thesis, and presents several areas in which additional work could take place, including industrial upscaling, improvements to tailoring, and advanced modelling methodologies that could be used for more accurately predicting microstructural development.

Chapter 2
State-of-the-Art in Hot Forming Die Quenching

Due to the increasing prevalence of UHSS in automotive manufacturing, the technology available to improve process efficiencies and, ultimately, manufacturability of complex components, is developing quickly. This chapter aims to outline the history of automotive steel usage, and the subsequent invention, application and proliferation of HFDQ technology. It also discusses several state-of-the-art innovations in the field of rapid austenitization, including electrical resistance (Joule) heating, induction heating, roller hearth optimizations, and direct contact heating.

2.1 Brief History Automotive Steel Forming

In the 1950s and 1960s, automotive steel manufacturing was driven by the development of steels with excellent deep-drawing properties that could be formed into increasingly complex patterns [16]. For these applications, plain mild steels were formed, primed, and painted; unfortunately, with the lack of any protective barrier for the steel, corrosion resistance of these automobiles was poor. This was remedied in the 1970s with the development of hot-dip and electro-galvanizing lines, and by the 1980s, two-sided galvanized steel became the industry standard [17].

Hot forming was invented and patented in 1977 by the Swedish company Plannja for the processing of saw and lawn mower blades [18]. Saab Automobile AB was the first automotive manufacturer to employ hot stamping in 1984 for forming a martensitic component for the Saab 9000 [18]. The advantage initially presented by hot-formed components was substantially higher strength compared to the mild steels traditionally used in the automotive industry, while simultaneously allowing for thinner material cross sections to be used. In recent years many governments have implemented stringent CO_2 emission standards in order to combat accelerating climate change. It has been suggested in the literature that a 10% reduction in net vehicle weight can translate to improvements to fuel economy by 6-8% [19]. To work towards these new standards, automotive companies are beginning to create a greater number of hot

formed components to further reduce the weight, and, in turn, improve the fuel efficiency and reduce emissions.

2.2 Hot Forming

Hot forming of steel is a process in which a steel is transformed into a single-phase (austenitic) solid solution through heating. At this point, the metal is simultaneously formed into the desired shape and quenched. Forming steel while it is fully austenitic is advantageous because the increase in ductility resulting from austenite's FCC crystal structure and reduced flow stress from the heightened temperature allow for a lower applied force to be used to form the final part when compared to that required for cold work [12]. Comparatively, cold forming processes use room-temperature steel that is blanked and formed directly from a roll of steel; this process is unable to induce solid state transformations within the material. Additionally, because of the high strength and low ductility of martensite at room temperature, simultaneous forming and quenching allow for the creation of geometries that would be otherwise impossible to achieve with traditional cold-forming.

In contrast, cold forming can also lead to inconsistent properties within the metal as only certain areas of the cross section are subjected to strain hardening. This can compromise the strength of the as-formed part, and may require subsequent heat treatment, which is costly and time-consuming. In addition, hot forming also reduces, if not eliminates, any spring back in the part during forming [20].

2.3 Usibor® 1500P

Usibor® 1500P is a 22MnB5 steel with a protective Al-Si coating manufactured by ArcelorMittal; it is one of the most prevalent UHSS used in hot forming. The chemical constituents of the steel, as provided by the manufacturer, are given in Table 1. The presence of boron in the steel causes the bainite "nose" of the time-temperature transformation (TTT) diagram to shift to the right, as shown in Figure 2, allowing for the formation of a fully-martensitic crystal structure in the stamped parts at lower quenching rates. The Al-Si binary coating protects the steel substrate from oxidizing and decarburizing in the furnace. The

coating also melts at approximately 575°C and then reacts with iron that diffuses from the substrate steel to transform into a permanent Al-Si-Fe layer that provides additional corrosion protection.

Table 1 - Nominal chemical composition of the steel substrate of Usibor® 1500P (wt.%).

C	Mn	Cr	B	Ti	Al	Si	Fe
0.24	1.21	0.2	0.0031	0.036	0.04	0.28	Bal.

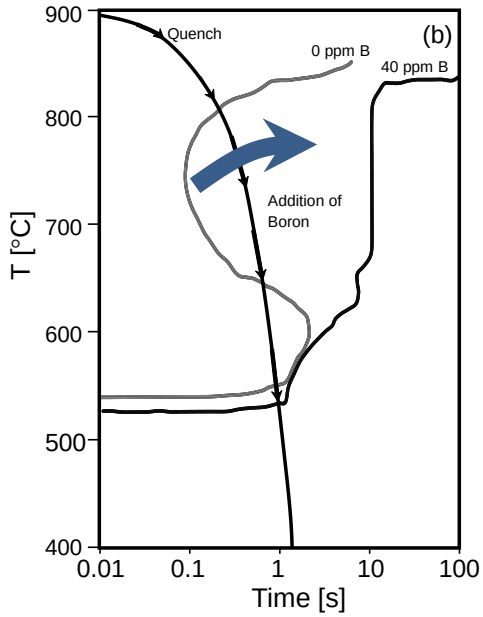

Figure 2 - Hypothetical TTT curve for low carbon steel, which shows how adding boron shifts the bainite "nose" to the right, reducing the quenching rate needed to form martensite. (Adapted from Babu et al. [21].)

2.4 Current State-of-the-Art in Heating Technology

2.4.1 Industry Standard: Roll-Through Hearth Furnaces

Roll-through hearth furnaces are by far the most common heating technology presently used in industry for heating sheet metal for HFDQ applications. These furnaces consist of a well-insulated heating chamber, high-temperature-resistant rollers, a heating source (electric, gas, etc.), and an array of sensors, servos, and controllers. Furnace sizes vary from application to

application, as they are sized according to mill productivity, required slab heating time, dimensions of the material to be processed, and any other buffer time requirements [22].

Because of the nature of roll-through design, the heated chamber must be long enough to ensure that the blanks fully austenitize, and in the case of coated steels, that the coating fully transforms into its desired form. The average length for most roller hearth furnaces is around 30-40 meters, but they can be made much larger [18]. As a benchmark, Thermo Transfer Inc. designs their furnaces to have a maximum temperature range of 950-1200 °C [23]. Karbasian and Tekkaya [18] shows that the thickness of the blank material being processes has a substantial influence on the minimum time required in a roller hearth furnace treatment regime to attain a fully austenitic structure prior to forming and quenching, as can be seen in Figure 3. While it is possible for the blanks to become fully austenitized in 2 to 4 minutes in a furnace, most manufacturers allow them to soak for several additional minutes to allow for austenite grain growth, Al-Si-Fe coating development, and to ensure a homogeneous temperature distribution throughout the blank.

The presence of the Al-Si coating on the blanks does present an issue for roller hearth furnaces: over time, the coating tends to adhere to the rollers, as shown by [1]. As more Al-Si gradually adheres, rollers can crack and shatter, especially during shut-down periods. Broken rollers can be expensive to replace, and add to the overall cost of operation for these furnaces.

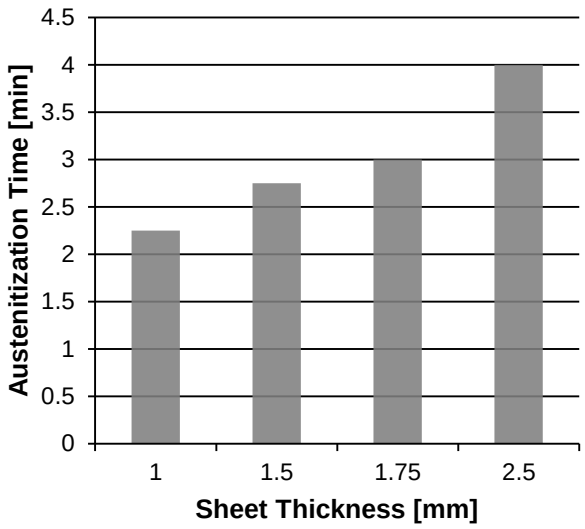

Figure 3 - Required processing time within a roller hearth furnace in order to fully austenitize blanks of various thicknesses. Adapted from [18].

2.4.2 Resistance Heating

Mori et al. [24, 25] describe electrical resistance heating, in which the blank is placed between two electrodes and then austenitized by electrical resistance (Joule) heating at a rate of 400 K/s. In resistance heating, an electrical current is passed through the steel blank between two electrodes. A combination of a restriction in the cross sectional area of the zone being heated and the native resistance of the steel blank cause the blank to heat up as the current passes through it. The maximum temperature of the steel blank can be controlled by the input power. For several tests discussed in later chapters of this work, the Gleeble® 3500 thermomechanical testing apparatus was used, which operates according to a similar principle.

Electrical resistance heating can be readily integrated into a stamping line by combining the heating and forming die into a single set, as seen in Figure 4. This allows for greatly reduced the transfer time from the heating to the forming operation; Mori et al. were able to achieve a transfer time from 5 seconds for a hearth furnace down to 0.2 seconds with a resistance heating apparatus [24].

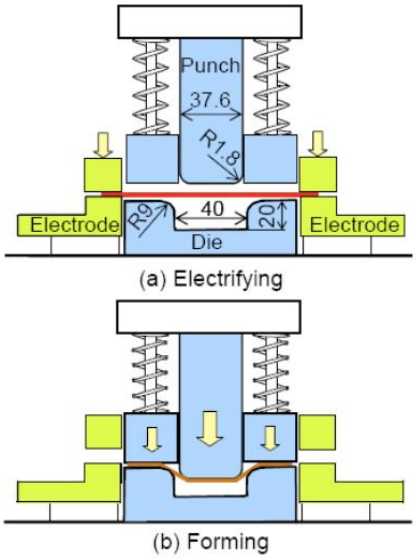

Figure 4 - Electrical resistance heating and stamping arrangement proposed by [24].

Unfortunately, this approach requires a large electrical resistance between the electrodes, and thus is only suitable for long and narrow blank geometries through which the electrical current can be restricted in order to generate sufficient heat. Additionally, from an industrial perspective, it is would be necessary to heat blanks that have been cut and trimmed into non-uniform, complex shapes in their relatively soft and ductile as-received state. As such, balancing current densities to achieve uniform heating would present a significant challenge for these parts. Moreover, this technique would also likely require unique rigs designed for each specific part that have been specially tuned to apply the appropriate current for each geometry. Finally, because the electrical resistivity of metals depends strongly on temperature, this process often causes considerable temperature variation along the length of the component, resulting in undesired variations in austenitization and mechanical properties throughout the stamped parts. This would also present a challenge for the tailoring of mechanical properties, since the non-uniform distribution of heat would be difficult to control in narrow blank regions.

2.4.3 Induction Heating

Induction heating is commonly used for the melting, tempering, and heat-treating of metals, as well as in the assembly and packaging industries [18]. Kolleck et al. [26] suggested that

induction heating may be used to heat blanks for HFDQ applications. A strongly fluctuating magnetic field is generated by alternating the voltage supplied to an induction coil. This magnetic field induces eddy currents within the blank, which, in turn, results in Joule heating. The heat generated in the blank is controlled by the frequency of the induced current as well as the material properties such as magnetic permeability and electrical conductivity [27].

The frequency of the induced current affects the penetration depth of the magnetic field, and thus defines the heat affected area (i.e. to define the thickness of a surface hardened layer). High frequencies result in a low penetration depth, and low frequencies to a high penetration depth. The three main types of induction coils (longitudinal, transverse, and face field inductors) produce magnetic fields having differing properties and efficiencies. In general, longitudinal inductors provide a more uniform temperature distribution than face inductors; however, both may be required in order to achieve the required heating temperature [26]. The heating rate for a longitudinal inductor is primarily controlled by the feed rate whereas the distance between the inductor coil and the steel blank is the governing parameter for face field inductors.

Induction heating is primarily used to heat objects with a high length to width ratio. Objects such as pipes with a smaller diameter compared to length of the pipe lend themselves to induction heating. One of the problems with induction heating is the concept of the reference depth, the theoretical minimum depth of heating that a frequency will produce for a given power and work piece temperature. The cross-sectional size must be at least four times the reference depth in order to avoid current cancellation [28]. This becomes problematic when heating thin sheets, since a very high frequency would need to be generated to avoid this issue.

While this technique is generally more energy efficient than roller hearth furnaces, it is again difficult to achieve uniform heating through the blanks, particularly for complex blank geometries [18]. Finally, because the as-received blanks possess a BCC pearlitic/ferritic structure, they are ferromagnetic, and could potentially be deformed or jammed in the strong magnetic field required to induce heating.

2.4.4 Direct Contact Heating

Ploshikhin et al. [29] recently proposed a direct contact heating technique in which blanks are austenitized by heating them between two hot plates, themselves heated through magnetic induction. As with the other non-radiative approaches, direct contact heating requires considerably less floor space, as the heated plates could be installed as an in-line process within existing stamping line. Also, with this large reduction in the area of the heating medium (~1 m^2 versus >60 m^2), the process would be far more energy efficient compared to furnace-based heating. For this application, uniformly heated plates were used to compress the blanks in order to transfer heat from the plates into the blank. The experimental apparatus they used is shown in Figure 5.

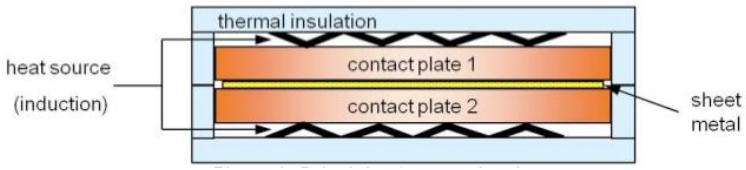

Figure 5 - The direct contact heating apparatus used by Ploshikhin et al., 2009 [29].

Ploshikhin et al. heated steel blanks to the austenitization temperature using a pilot direct contact heating apparatus, quenching them on a flat, cooled die. The sample steel blanks tested had dimensions of 210 x 120 mm and reached temperatures up to 1050 °C. This maximum temperature was limited by the maximum service temperature of the induction-heated plates [29].

As noted above, most HFDQ is done on coated steels such as Usibor 1500 P, [20]. It is imperative that the heat treatment of this steel does not damage the surface coating. Considering the nature of direct contact heating and the presence of the Al-Si coating, having a heated striking surface in constant contact with the material being processed poses a risk of molten coating adhesion to the surface. However, Ploshikhin et al. present promising results in this regard; Figure 6 (a) and (b) show the coating microstructure before and after heat treatment in a traditional furnace for approximately 7 minutes. In comparison, Figure 6 (c) shows the coating microstructure after only 60 seconds at 940 °C. It was also demonstrated

that even shorter heating times could be accomplished by increasing the operating temperature. Figure 6 (d) shows the coating microstructure after heating at 1020 °C [29].

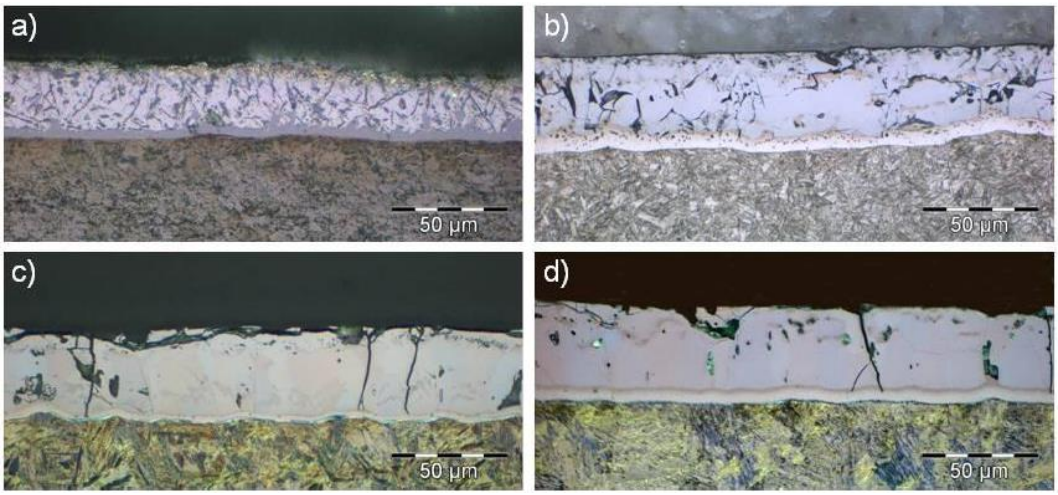

Figure 6 - Microstructure of the Al-Si coating (a) before heat treatment, (b) after furnace heat treatment, and after direct contact heating at (c) 950 °C and (d) 1020 °C [29].

Preliminary results from this study suggested that this technique can produce fully-austenitized blanks with a mature Al-Si-Fe coating within approximately 30 seconds. Comparatively, traditional furnace heating generally requires between 4 to 10 minutes to accomplish the same tasks.

2.5 Tailoring of Mechanical Properties

The tailoring of mechanical properties is one of the focal points for the international hot forming community. Generally, tailoring techniques focus on treatment of steels after forming, ranging from direct flame impingement [30] to selective in-die [31, 11] and out-of-die [32, 33, 34] heating have been successfully employed to induce a tailored microstructure, albeit often facing issues with dimensional stability and transition zone length. Relatively little work is done on the tailoring of material properties on the heating side. However, as previously mentioned, Wilsius et al. [14] has successfully utilized heat shields to selectively heat coupons, and Stöhr et al. [15] performed successful patched heating experiments.

Presently, one of the challenges facing many groups is reducing the transition zone between the fully hardened and ductile zones. Generally, this is a by-product of the selective quenching methodology; Behrens et al. achieved a 50 mm transition using out-of-die water-air spray [32], while a high-volume laser softening approach offers a slimmer 15-20 mm transition, albeit through the use of expensive high powered laser trimming technology [33]. Schwartz GmbH is presently developing an out-of-die 'thermal printer' designed to be integrated in between the furnace and press which has demonstrated a 30 mm transition zone, with excellent repeatability and 15-20 second cycle times [34].

2.6 Summary

While a great deal of work has gone into researching alternative heating methodologies, it is apparent that direct contact heating presents the most feasible approach to develop a rapid heat treatment technology. This is due to its scalability, its relative simplicity in design and ease of construction, its ability to be installed in-line in an existing stamping operation, and finally, the potential for tailoring material properties. Additionally, the successful results reported by Ploshikhin et al. [29] lends credence to the concept, and increases confidence in the likelihood of a similar technology achieving desirable results.

Chapter 3
Design & Modelling of a Direct Contact Heating Monolith

From the recommendation presented in Chapter 2, this chapter will discuss the detailed design and mathematical modelling of a direct contact heating monolith. The design limitations are presented and discussed in the context of the final design. The heat transfer principles used in the design are explained and demonstrated. The final design, and fully-constructed lab-scale heated monolith are presented.

3.1 Design Considerations

Before exploring more detailed design aspects, it is necessary to identify the key criteria by which the ultimate success of this endeavor will be judged. The following criteria were identified in conjunction with our research partner, F&P Manufacturing Inc., and must be satisfied in order to consider this work a viable alternative to traditional roller hearth furnaces:

1. The heated monolith must be fully integrated into an existing stamping line, requiring minimal additional space. A conceptual process flow for the formation of a B-pillar is shown in Figure 7;
2. The material processing time (*i.e.*, the time required to austenitize the blanks) must be shorter compared to current furnace-based processes;
3. The monolith heating method must consume less energy than furnaces;
4. The Usibor® 1500P blanks must be fully and uniformly austenitized, by heating them beyond the austenitization temperature (T_{Ac1} = 880 °C) as shown in Figure 11;
5. The surface coating of the Usibor® 1500P blanks must be fully transformed and intact at the end of the heating process.

These requirements are the driving force behind the design considerations discussed in the following sections. Also, the laboratory space available for testing imposes further constraints that must also be acknowledged and incorporated into the design process.

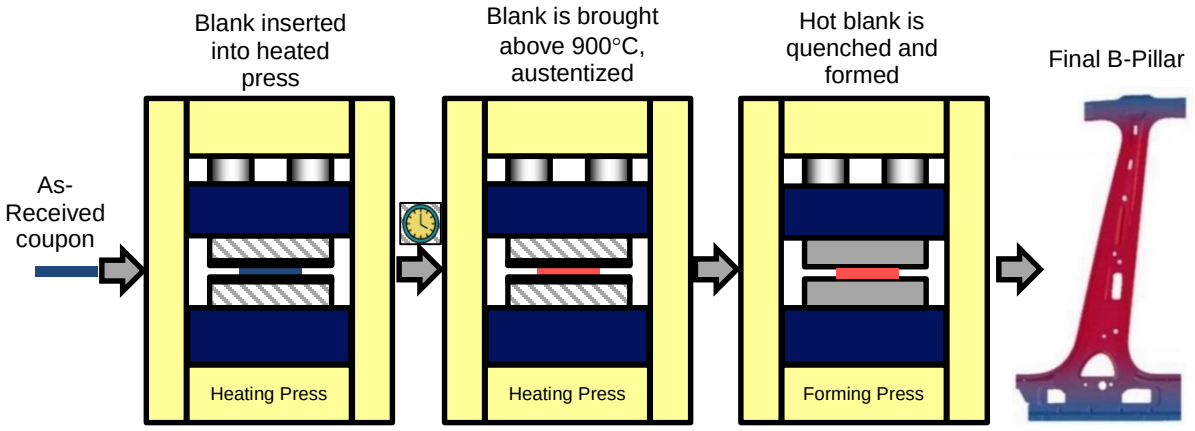

Figure 7 - Hypothetical direct-contact HFDQ process for a B-pillar.

3.1.1 High Pressure Lab Utility Limitations

The laboratory used for experimentation in this work is the University of Waterloo's High Pressure Laboratory. The lab is equipped with three 208V-30A breakers routed through thermocouple-controlled proportional-integral-derivative (PID) controllers. Unfortunately, the lab is not equipped with a ventilation system suitable for safely evacuating harmful combustion byproducts from the area. As such, it was not possible to consider heating methodologies involving direct or indirect heating via gas combustion.

3.1.2 Hydraulic Press

The High Pressure Lab contains an 890 kN Macrodyne high-speed hydraulic press to which the direct contact heating apparatus is mounted. Being able to minimize the pressure applied to the monolith increases the number of materials potentially available for use in the construction of the heated die, as ones with lower compressive strength, but superior thermal effusivity, could be employed. However, the load cell attached to the hydraulic press is not sufficiently accurate at pressures lower than 130 kN, and it is therefore necessary to consider materials with compressive strengths greater than this limit in order to avoid accidentally crushing the monolith during operation.

3.2 Heat Transfer Modelling

3.2.1 Surface Temperature, Heat Flux, and Thermal Effusivity

Because the monolith will be heated internally, and maintained at a constant internal temperature, the rate of heat transfer from the surface of the monolith to the test coupons can modelled by approximating the striking surface as a semi-infinite solid. When the room-temperature coupon is placed upon the striking surface, there will be a transient thermal response resulting from the induced thermal gradient. As such, the transient energy equation at the striking surface (i.e., $x = 0$) is given by the partial differential equation [35]:

$$\alpha \frac{\partial^2 T}{\partial x^2} - \frac{\partial T}{\partial t} = 0 \tag{1}$$

By following the derivation and boundary conditions outlined in Appendix A, it can be shown that the temperature distribution within the blank is given by [35]:

$$T(x,t) = T(t_0) + \left[T_s - T(t_0)\right]\left\{1 - erf\left[\frac{x}{2(\alpha t)^{1/2}}\right]\right\} \tag{2}$$

And, by differentiating (2), applying the chain rule, and evaluating the resultant at $x = 0$, the transient surface heat flux is found to be [35]:

$$\begin{aligned} q_{\rho c_p k}(t) = q_s(t) &= -k\left[T_s - T(t=0)\right]\left.\frac{\partial T^*}{\partial x}\right|_{x=0} \\ &= -k\left[T_s - T(t_0)\right] = -\frac{k}{(\pi\alpha t)^{1/2}}\left[T_s - T(t_0)\right]\frac{\partial \eta}{\partial x}\frac{\partial T^*}{\partial \eta} \\ &= -\frac{\left(\rho c_p k\right)^{1/2}}{\pi^{1/2} t^{1/2}}\left[T_s - T(t_0)\right] \end{aligned} \tag{3}$$

In the final form of the above equation, the quantity $\left(\rho c_p k\right)^{1/2}$ is defined as the thermal effusivity, with units of W-s$^{1/2}$ / m^2-K. Materials with high thermal effusivities allow for the transmission of large amounts of heat, and vice versa. This effect can be harnessed to tailor the heating rate allowed for by the striking surface of the heated monolith by varying the materials

used in the construction of the monolith itself. Similarly, by incorporating materials with different thermal effusivities in a single striking surface, it would be possible to selectively vary the heating rate of a coupon, despite having a uniform striking surface temperature.

Finally, because the temperature of the striking surface will likely not remain constant throughout the heating of the coupons, it is necessary to re-define (2) and (3) such that any temperature changes experienced are captured in the model. If the temperature variation with respect to time is approximated as piecewise linear, the solutions for $T(x,t)$ and $q_{\rho c_p k}(t)$ are given by [35]:

$$T\left(x,t\right)-T\left(t_0\right)=\sum_{i=1}^{n-1}\left\{\begin{array}{l}\left[\left(a_i-a_{i+1}\right)\left(t+\frac{x^2}{2\alpha}\right)+\left(b_i-b_{i+1}\right)\right]\times \\ \left\{erf\left\{\frac{x}{\left[4\alpha\left(t-t_i\right)\right]^{1/2}}\right\}-erf\left[\frac{x}{\left(4\alpha t\right)^{1/2}}\right]\right\}-\frac{x}{2\alpha\pi^{1/2}}\left(a_i-a_{i+1}\right)\times \\ \left\{-\left[4\alpha\left(t-t_i\right)\right]^{1/2}\exp\left[-\frac{x^2}{4\alpha\left(t-t_i\right)}\right]+\left(4\alpha t\right)^{1/2}\exp\left(-\frac{x^2}{4\alpha t}\right)\right\}\end{array}\right\}+$$

$$\left[a_n t+b_n-T\left(t_0\right)\right]erfc\left[\frac{x}{\left(4\alpha t\right)^{1/2}}\right]- \tag{4}$$

$$\frac{a_n x}{2\alpha\pi^{1/2}}\left\{\left(4\alpha t\right)^{1/2}\exp\left(-\frac{x^2}{4\alpha t}\right)-x\pi^{1/2}erfc\left[\frac{x}{\left(4\alpha t\right)^{1/2}}\right]\right\}$$

$$
\begin{aligned}
q_{\rho c_p k}(t) &= \frac{T_s(t) - T(t_0)}{A_k R_{\rho c_p k}(t)} \\
&= k \frac{\partial T(x,t)}{\partial x}\Big|_{x=0} \\
&= \sum_{i=1}^{n-1} \left\{ \begin{array}{l} \left[(a_i - a_{i+1})t + (b_i - b_{i+1}) \right] \times \left\{ \left[\frac{k\rho c_p}{\pi (t - t_i)} \right]^{1/2} - \left(\frac{k\rho c_p}{\pi t} \right)^{1/2} \right\} - \\ \frac{\rho c_p}{2\pi^{1/2}} (a_i - a_{i+1}) \left\{ -\left[4\alpha (t - t_i) \right]^{1/2} + (4\alpha t)^{1/2} \right\} \end{array} \right\} - \\
&\quad \left[a_n t + b_n - T(t_0) \right] \left(\frac{k\rho c_p}{\pi t} \right)^{1/2} - a_n \left(\frac{k\rho c_p t}{\pi} \right)^{1/2}
\end{aligned}
\tag{5}
$$

where

$$a_n = \frac{T_{s,n} - T_{s,n-1}}{t_n - t_{n-1}},\ \mathrm{b}_n = T_{s,n} - a_n t_n .$$

Should the striking surface temperature, T_s, remain constant during operation, equations (4) and (5) will reduce to equations (2) and (3), respectively. Equations (4) and (5) reveal that the die effusivity is a key material parameter, even when the die temperature changes with time.

3.2.2 Monolith Heating and Heat Loss Calculations

A heat transfer analysis of the monolith at its maximum operating temperature (~1000 °C) predicted that approximately 6 kW of thermal energy would be lost to the surrounding environment while the die was in the closed position, primarily by heat conduction through the insulation and into the body of the hydraulic press (modeled as a semi-infinite thermal mass). A much greater rate of heat transfer occurs when the press is opened to transfer the coupon on to or off of the heated surface, as shown in Figure 8.

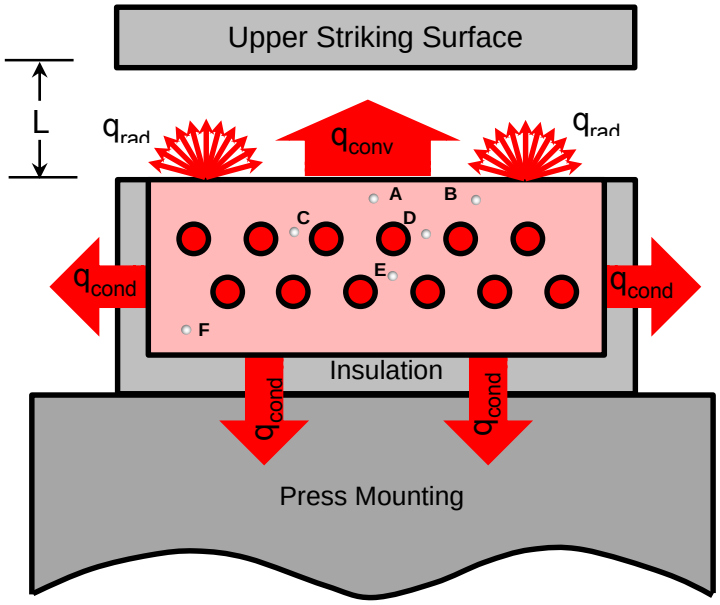

Figure 8 - Schematic showing heat losses from the monolith and thermocouple locations.

To quantify radiation losses from the striking surface, the view factor from the exposed hot monolith surface to the surroundings was calculated as a function of the separation distance between the upper striking surface and the lower heated surface using [36]

$$F_{surf-surr} = 1 - \left(\frac{2}{\pi XY}\right)\left\{\ln\left[\frac{\left(1+X^2\right)\left(1+Y^2\right)}{1+X^2+Y^2}\right]^{1/2} + X\left(1+Y^2\right)^{1/2}\operatorname{atan}\left(\frac{X}{\left(1+Y^2\right)^{1/2}}\right) + Y\left(1+X^2\right)^{1/2}\operatorname{atan}\left(\frac{Y}{\left(1+X^2\right)^{1/2}}\right) - X\operatorname{atan}\left(X\right) - Y\operatorname{atan}\left(Y\right)\right\} \quad (6)$$

where the length and width of the heated monolith surface are x = 0.25 m and y = 0.3 m, respectively, the separation distance is L, and $X = x/L$, $Y = y/L$. Assuming that the upper surface is approximately the same temperature as the monolith face, radiant losses from the monolith is then given by

$$q_{rad} = A_{surf} F_{surf-surr} \varepsilon\sigma\left(T_{surf}^4 - T_{surr}^4\right) \quad (7)$$

where $A_{surf} = xy = 0.075$ m^2, the emissivity is taken to be 0.85 (typical a conservative estimate for the emissivity for oxidized nickel at a high temperature [37]), $\sigma = 5.67 \times 10^8$ W/(m^{2}K^4) is the Stefan-Boltzmann constant, and $T_{surr} = 298.15$ K (25°C).

Natural convection losses from the exposed surface were found using Newton's law of cooling:

$$q_{conv} = \bar{h} A_{surf} \left(T_{surf} - T_{\infty} \right) \tag{8}$$

where $T_{\infty} = T_{surr}$. The convection coefficient is derived from [38]:

$$\overline{Nu}_L = \frac{\bar{h} L_c}{k} = 0.54 Ra_L^{1/4} \tag{9}$$

with

$$Ra_L = \frac{g\beta \left(T_s - T_{\infty} \right) L_c^3}{\alpha \nu} \tag{10}$$

The characteristic length in Equations (9) and (10) is given by $L_c = A_{surf}/P = 0.0857$ m, while the properties of air are evaluated at the film temperature, $T_f = (T_{surf}+T_{\infty})/2$. The predicted losses found from natural convection and radiation are plotted in Figure 9 as a function of L. It is clear that controlling the opening height is crucial to minimize heat transfer losses during coupon transfer.

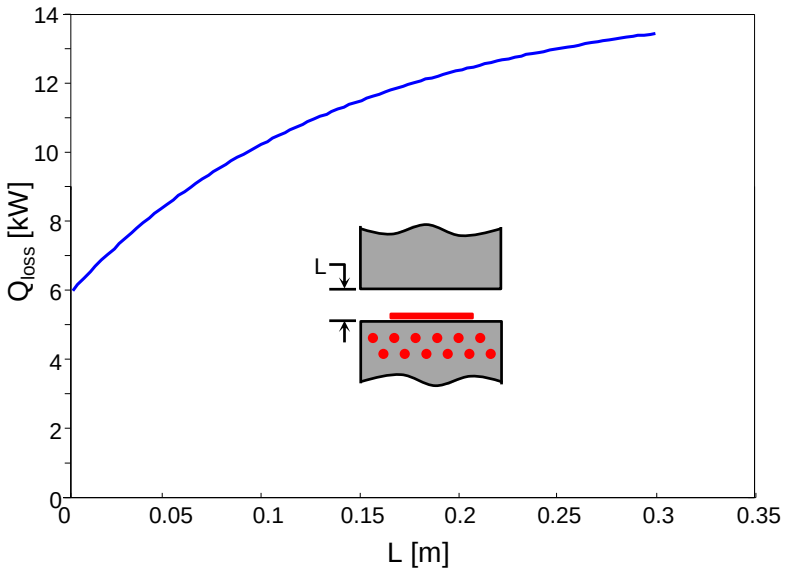

Figure 9 - Predicted heat losses from the monolith as a function of opening space, L.

3.3 Material Selection

The monolith material must be resilient to oxidation and have reasonable compressive strength at high temperatures. Both metallic and ceramic materials were considered: among metallic materials, Ni-Cr-Fe alloys were found to be the most suitable, and RA330® (35Ni-19Cr-1.25Si) was ultimately chosen. RA330® was found to possess excellent high-temperature thermomechanical properties (compressive strength, thermal conductivity, thermal expansion, etc.). Comparatively, Inconel® 601 presented marginally superior high-temperature thermomechanical properties, but costs approximately three times that of RA330. A custom-sintered alumina monolith was also considered, as it has excellent high-temperature resistance to corrosion (considering it is already and oxide), a high specific heat capacitance, and is an electrical insulator. Unfortunately, manufacturing a custom-sintered Al_2O_3 monolith proved cost-prohibitive, and the lower thermal effusivity of alumina would have required a longer heating time in order to fully austenitize the coupons.

3.3.1 1D Heat Transfer Model

Initial coupon heating simulations were carried out with an implicit 1D finite-difference heat conduction model, using temperature-dependent thermophysical properties for Usibor® 1500P and RA330®, Inconel® 601, and alumina [20, 39]. A heat transfer coefficient of 4,000 W/(m^{2}K) was assumed between the coupon and the striking surface, based on experimentally-characterized heat transfer coefficients during the HFDQ forming stage carried out by Caron et al. [40]. The top of the blank (i.e., the upper striking surface-blank interface), and the bottom of the die were modelled as adiabatic Robin boundary conditions. 10 nodes were utilized for the blank, and 20 for the die. Uniform node spacing was used in the blank; non-uniform spacing was use the first 12 nodes in the die, with the remaining 8 being evenly spaced. For an initial monolith temperature of 1000˚C, the 1D simulation predicted that a 2 mm thick Usibor® 1500P coupon could reach the austenitization temperature of 950˚C within 15 seconds, thereby fulfilling one of the key functional requirements for direct contact heating defined above. This result suggested that the minimum set point temperature that the monolith be set to be 1000 °C. The comparative results of the three simulations is found in Figure 10.

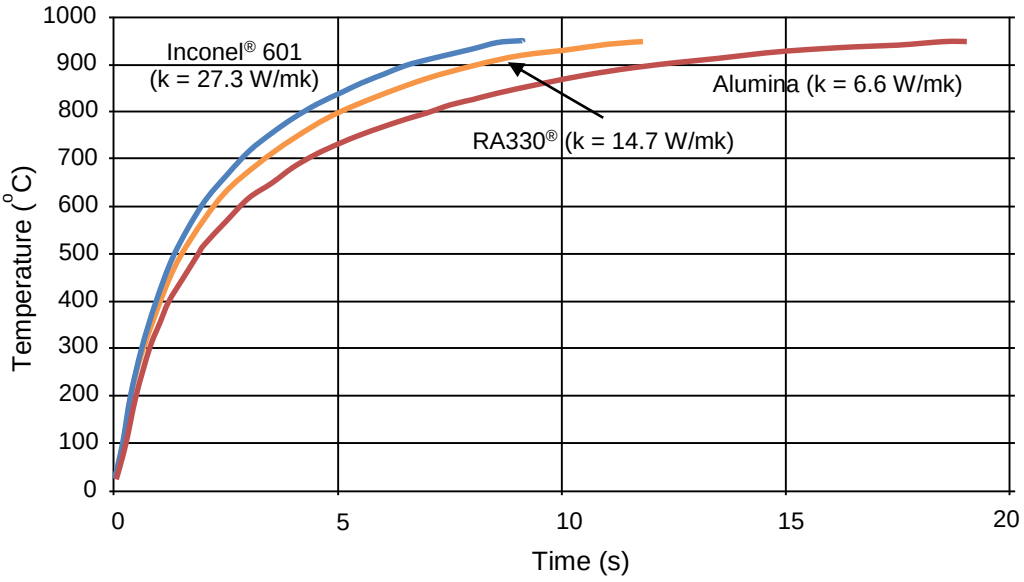

Figure 10 - Comparison of heating rates for Inconel® 601, RA330 ®, and alumina.

The monolith insulation was a combination of RSLE® 57 (silicon dioxide-based) and Zircal® 95 (calcium silicate hydrate-based) ceramic insulations, which have thermal conductivities of 0.6 and 0.3 W/(m·K), respectively; these insulating materials were chosen mainly for their stability at high temperatures, mechanical resilience, and superior machinability. Of the two insulations, RSLE® 57 had the higher service temperature, and consequently was used for all of the insulation in direct contact with the monolith, while the Zircal® 95 was used for secondary insulation.

3.4 Monolith Heating

As Naderi et al., 2008 [41], note, the blank must reach temperatures exceeding 880°C to surpass the Ac3 line of the Usibor® 1500P phase diagram, shown in Figure 11, in order to ensure that the as-received ferritic structure fully transforms into austenite, the solid-state precursor to martensite.

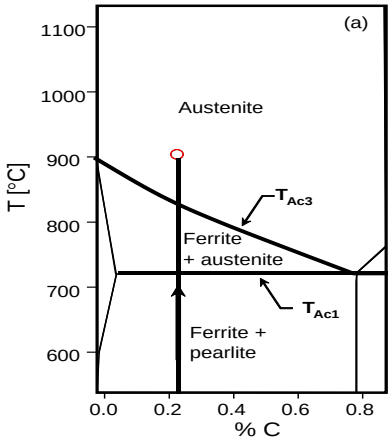

Figure 11 - Phase diagram for 22MnB5 steel.

The 1D heat transfer model discussed in the previous section showed that the monolith design temperature should be at least 1000°C in order to satisfy this requirement. Maintaining this monolith temperature in a safe and industrially-practical fashion can only be realized through a limited number of methods, including electrical resistance heating, magnetic induction heating (following [29]), and indirect gas fire heating.

Heating the die with a series of embedded electrical heating elements instead of indirect gas fire heating is an appealing choice, as this forgoes the need for complex and expensive safety equipment (ventilation, manifolds, etc.) required for indoor natural gas combustion. While magnetic induction has been shown by Ploshhikin et al. [29] to be an effective means of heating the monolith, it was not pursued in this work due to its greater complexity and capital cost.

Options for electrical heating elements are limited by the monolith operating temperature, which, in turn, is dictated by the austenitization temperature of Usibor® 1500P. This temperature exceeds the maximum service temperature of most "off-the-shelf" cartridge heaters, which is approximately 600°C. Molybdenum disilicide ($MoSi_2$) elements are capable of exceeding the maximum required operating temperature, but also require a step-down transformer to reduce the line voltage and increase the current from the electrical supply. $MoSi_2$ elements also tend to sag excessively at high temperatures, presenting the possibility of having an element come into contact the monolith, thus causing the system to become electrically ungrounded. As this presents a safety risk to the operator and a damage risk to the equipment, $MoSi_2$ elements were eliminated from the selection process.

Silicon carbide (SiC) elements were ultimately chosen for this application for their high-temperature rigidity and cost-effectiveness. Additionally, it was possible to install them in a simple series circuit using the 208 V, 30 A lines available in the High Pressure Lab. The heating elements were electrically isolated from the monolith with alumina tubes at the entrance and exits of the holes transecting the monolith.

Accordingly, twelve SiC elements with a net heating capacity of 10 kW were selected to heat the monolith; the excess heating capacity compared to the modeled losses of 6 kW was chosen to allow the monolith to reach its operational temperature quickly from startup, and to ensure that it will quickly stabilize after each cycle. The elements were installed in two banks, as shown in Figure 8, using two separate 208 V, 30 A lines. The banks were staggered in the die to minimize space taken up by the elements; this minimizes the total volume of the monolith, thus reducing the thermal mass of the system and consequently the time to reach operating temperature. Additionally, closely spaced elements promote a more uniform striking

surface temperature, which is essential to achieve uniform austenitization and uniform material properties in the quenched coupon. That being said, it was necessary to analyze the structure with a numerical model to ensure the thin material cross sections in the die would support the forces exerted when the heating die is closed around the coupon.

3.5 Interchangeable Striking Surfaces

As noted in Chapters 1 and 2, the Al-Si coating of Usibor® 1500P starts to melt at approximately 575°C and then reacts with iron that diffuses from the steel to form a permanent Al-Si-Fe layer [42]. Initial testing showed that the molten coating caused the coupons to adhere to the monolith, complicating coupon extraction from the die set, and promoting fouling of the striking surfaces. (As noted in Chapter 2, this is also a well-known problem experienced by the rollers in roller hearth furnaces, see e.g. [1]). In order to prevent the adhesion of the Al-Si to the monolith stamping surface, five interchangeable candidate striking surfaces were evaluated:

1. A highly polished RA330® surface;
2. A boron nitride (BN) aerosol coating;
3. A Metco® Diamalloy® 3001 cobalt-based superalloy;
4. A Metco® 410 nickel aluminide cermet; and
5. A combination coating of Amdry® 995 MCrAlY and Metco® 204 zirconia ceramic.

These coatings were chosen for their low coefficients of friction and low wettability to molten aluminum. The high polish surface was chosen to see if a smoother surface would reduce mechanical adhesion due to microscale roughness

3.6 Heat Transfer Modelling

A more elaborate finite element analysis was carried out to determine how the die would expand and contract during heating and cooling, to verify that the monolith was mechanically-sound under load, and to assess temperature uniformity of the monolith surface, which is needed to achieve uniform blank heating. A heat flux was specified over the inner surface of the heating element holes based on the manufacturer specifications of the SiC heating

elements. All of the insulation and structural steel was assumed to be in thermal contact with the heated monolith, and radiation and natural convection boundary conditions were specified over the exposed surfaces. The center plan of the domain was modelled using a symmetry boundary condition. A grid refinement study showed that the predicted temperature became grid-independent when using 29,585 elements, so further analysis was carried out using this level of refinement. The stress and temperature distributions can be seen in Figure 12 (a) and (b).

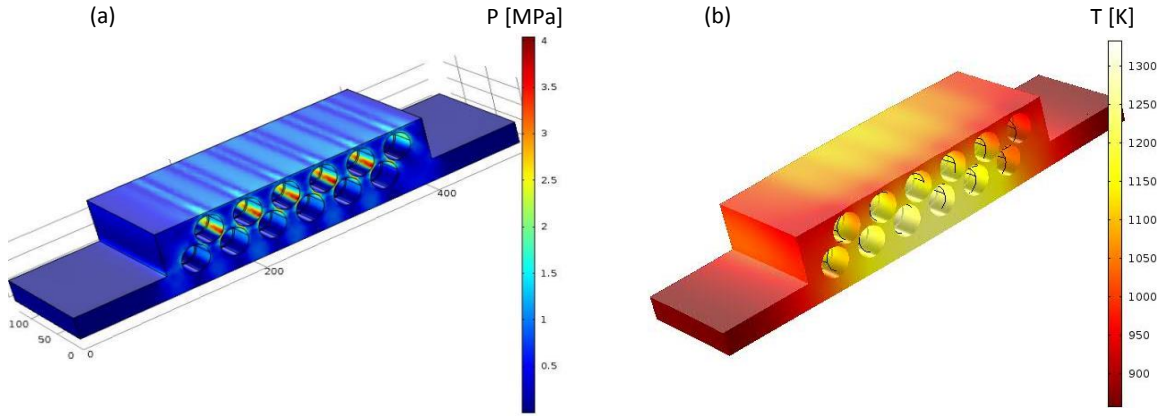

Figure 12 - (a) Modeled stress distribution and (b) temperature distribution.

As noted previously, the heating elements should be spaced as close together as possible to provide uniform heating and minimize the monolith volume, but the boreholes must also be sufficiently large to allow for monolith expansion and contraction without fracturing the SiC heater elements. The FEM simulation verified that the stress in the critical locations between the boreholes (~3.3 MPa) is far below the compressive strength of the material (138 MPa), and also verified that the heating element arrangement resulted in satisfactory temperature uniformity over the striking surface.

3.7 Final Design

The basic concept of the die assembly was to have a heated RA330® section encased in refractory board to maximize thermal energy retention. The heated die was mounted to the hydraulic press on a tool steel base plate using threaded studs with a T-nut at one end that

slides into the T-slots on the press. The heated surface was chosen to be a 30 cm x 25 cm rectangle; this was determined to be an efficient size for a lab-scale apparatus, since a minimum specimen length of 15 cm is required to perform tensile tests, and minimizing the volume of the monolith minimized the required heat input to reach the desired temperature. Figure 13 shows a SolidWorks mock-up the overall assembly of the heated die.

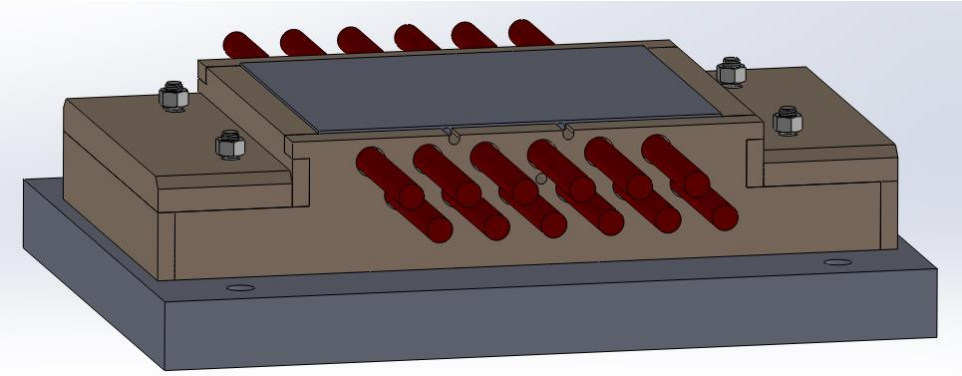

Figure 13 - Isometric view of heated die assembly.

Starbar® SE silicon-carbide heating elements, manufactured by I-Squared-R, shown as red cylinders in Figure 13, were chosen as the heat source for their cost and ease of installation. A schematic representation of a Starbar® SE element can be seen in Figure 14. The heaters have a 25.4 cm-long spiral-cut hot zone surrounded by two 15.25 cm-long solid cold zones with aluminized ends to promote electrical conductivity, as noted in Figure 14. The elements have a diameter of 1.9 cm. This geometry results in a heated zone surface area of 151.6 cm^2 per element. The nominal resistance of these elements is 1.57 Ω, ±20%. The spiral cut in the heated zone allows for a marked decreased cross-sectional area, which is responsible for the Joule heating effect. The solid zones are cooler than the spiral-cut heating zones due to their larger cross-section and lower electrical resistance. The elements were then connected in series via braided wire made of high-temperature-resistant stainless steel.

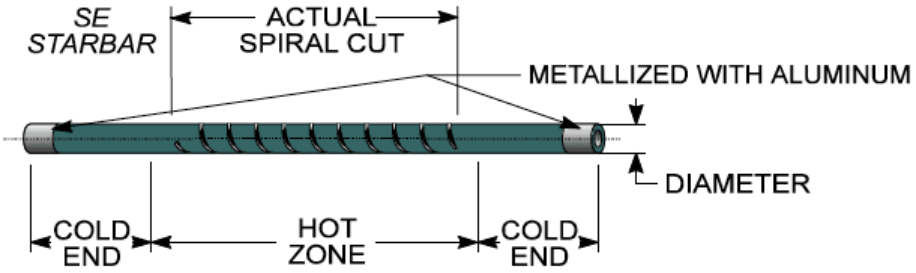

Figure 14 - Starbar® SE SiC heating element used to heat the monolith [43].

Based on the geometry of the heating elements, the power output density per element and requisite current capacity was calculated as shown in Appendix B. Recalling that a net power output of 10 kW was required to ensure any losses are overcome, an output of 833.33 W/element was necessary. At 220 V, this would require at least 23.04 A to be available to power a bank of six elements. Fortunately, the High Pressure Laboratory had three 220V, 30A breakers available to power each bank of elements.

One of the critical design aspects for the monolith was the positioning of the silicon-carbide heaters. Placing all twelve heaters in the same plane was initially considered; it quickly became apparent, however, that the manufacturer's recommended heater spacing (twice the diameter between elements) could not be achieved without significantly increasing the size of the heated surface. To compensate for this, two rows of six heaters were placed off-center from each other in an attempt to distribute the heat input evenly throughout the interior so to minimize non-uniform temperature distributions as much as possible. High-temperature, ungrounded K-type thermocouples sheathed in a 6.35-mm-diameter temperature-resistant nickel-chrome OMEGACLAD® material were used to control the power input to the heaters. These thermocouples were installed in locations C and E, shown in Figure 8. These thermocouples were routed through two proportional-integral-derivative (PID) controllers (one per bank) that automatically controlled the heat input to the monolith. The remaining thermocouple locations were used to monitor and record the temperature in real-time by a custom-built data acquisition (DAQ) device. By placing the control thermocouples in the locations shown in Figure 8, any process variations experience by the system (opening/closing the die set, inserting a room-temperature blank, etc.) would not drastically affect the control of the system. Hard-wired

over-temperature thermocouples was also installed inside the junction boxes to ensure the electrical equipment stayed well below its upper limit operating threshold.

As shown in Figure 13, the heating elements extend beyond the die. While the volumetric heating in these portions is very small compared to the heating sections due to their larger cross-section, they still reach temperatures exceeding 300 °C due to axial conduction of heat from the element heating zones, and, as such, they must be isolated for both thermal and electrical safety. Boxes made from Zircal® 95 were built to surround each bank of heaters and their electrical connections. Small holes were drilled into the top of the box to allow for some ventilation to prevent the box from overheating. An insulating ceramic blanket was placed in between each of the heaters, as well as underneath each element running through the monolith as an additional means for electrical isolation. The green rings around the heating elements, as seen in Figure 15, represent 50-mm-long custom-sintered alumina tubing that was used to provide non-conductive, rigid support for each of the heating elements.

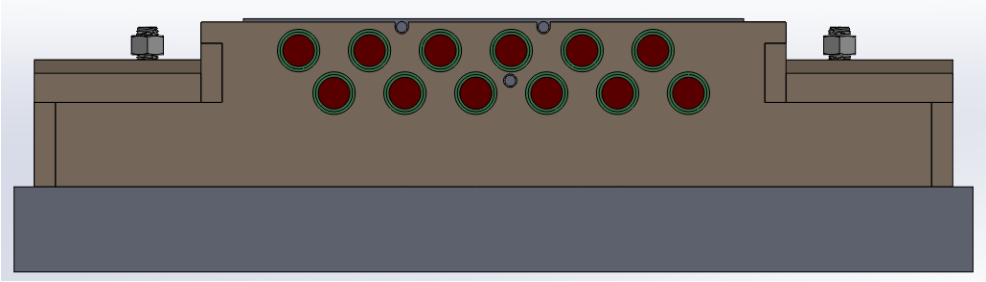

Figure 15 - Front view of die assembly.

The heated die was mounted to the base plate using four ¾”, 316 stainless steel hexagonal head bolts. The hex head fit into a close fitted slot in the base plate, allowing the nut on the top of the bolt to be adjusted without requiring access to the bolt head on the underside of the baseplate. The bolts went through the flange of the heated die and were thermally isolated from monolith with an insulating sleeve. To allow for thermal expansion, two bolts were fixed to the base plate via a close fit clearance hole while the remaining two were placed in a slot, as seen in Figure 16. The slot allows for controlling the direction for expansion.

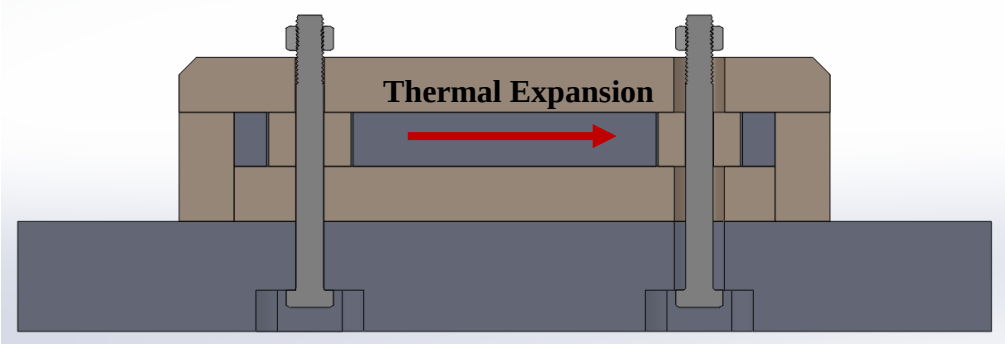

Figure 16 - Cross section of bolt location to account for thermal expansion.

The insulation was mechanically fastened together using interlocking tabs, shown in Figure 13. The tabs were used to provide a way of assembling the insulation, while still allowing the insulation to expand during the initial heating of the die.

The upper striking surface was the other major component of the complete die design. The upper die was numerically modeled as an adiabatic surface. Although this is a theoretical condition, and not achievable in practical applications, a sheet of the RSLE® 57 insulation, in addition to another layer of Zircal® 95, were used as the upper die surface. These two sheets of refractory board were fastened to a 0.75 in hot-rolled steel base plate using four "Z" brackets made from AISI 304 stainless steel. In order to both control the pressure exerted by the upper striking surface and ensure a uniform distribution of pressure, the surface was mounted on nitrogen springs set to exert a maximum force of 130 kN. The surface was installed so that it would float on guide rods, and the springs would compress accordingly as the ram descended. These springs were a necessary addition, as it was discovered early on that it was difficult to control the force exerted by the ram in displacement-control mode, due to the lack of sensitivity of the controlling load cell. It was found that a difference of fractions of a millimeter (i.e., any possible drifting of the ram) could cause concerning changes in the applied load. From [28], it was found that increasing the applied load did not have a substantial effect on increasing the heat transfer coefficient, and early testing found that larger applied loads (i.e., those in excess of 220 kN) would result in the coupon adhering to one of the striking surfaces. Maintaining a constant, relatively low-pressure for each test both improved data quality, and minimized the

adhesion issue initially experienced. Figure 17 shows the arrangement of the upper striking surface.

Figure 17 - Upper striking surface with primed nitrogen springs.

3.8 Final Assembly

The final assembly for the heating apparatus is shown in Figure 18, mounted in a 250 ton hydraulic press. The heated monolith remains stationary, while the upper refractory surface is raised and lowered for coupon loading and unloading. In the closed position the insulating upper surface reduces heat loss to the surroundings, and when the coupon is inserted into the press, it is heated from below by the RA330® monolith and from above by the hot RSLE 57® insulation. Since the focus of this work is on direct contact heating, heated coupons were quenched using a forced air quenching apparatus (FAQA) or oil to simulate quenching rates comparable to those obtained during the HFDQ forming phase. The apparatus was certified by the Canadian Standards Association (CSA) for safe electrical operation.

Figure 18 - Final die set assembly mounted in the 250 ton hydraulic press.

Chapter 4
Testing Methodologies

This chapter describes the experimental preparations, testing methodologies, and data sampling procedures used to characterize the functionality of the apparatus presented in Chapter 3. Alongside the final monolith design, this chapter will finish laying the groundwork for the overall experimental design.

4.1 Blank Preparation

In the present study, Usibor® 1500P sheet steel with an Al-Si coating was used as the testing material. Usibor® is commonly used in North America for hot forming applications, and was identified by F&P Manufacturing Inc. as the variety of steel that they woud ultimately be looking to heat treat. Coupons with dimensions of 100 mm × 200 mm and a thickness of 2 mm were machined from the Usibor® sheet steel for the tests. Usibor® is available in many gauge thicknesses, and the greater the thickness, the greater the challenge of attaining the desired internal temperature via direct contact heating. As such, F&P Manufacturing suggested we focus on the upper limit of what they would likely be heat treating with this technology once adapted for their facilities, thus testing focused on 2 mm-thick specimens.

4.1.1 Temperature Measurement

The coupon temperature was measured using a K-type thermocouple resistance spot welded into a 1 mm deep channel machined into each coupon. Since the coupon is heated from the top and bottom surfaces (although the thermal effusivity of the upper striking surface is approximately 10 times smaller than that of the heated monolith), the mid-thickness temperature is considered the minimum coupon temperature at any instant. The thermocouple wires were welded individually to the blank, resulting in an implicit thermocouple junction [40]. The thermocouple sheath was then secured with Pyro-Putty® 2400 thermal paste that was rated to 1100 °C [44]. This paste was used, instead of a more rigid high-temperature epoxy, so that stresses on the thermocouple sheathes were minimized, as the thermocouple wires themselves were fragile and easily broken.

4.2 Quenching Methodologies

Hot forming typically requires the use of a set of dies to perform the quenching stage of the process such that the rate of cooling is greater or equal to the critical quenching rate of 27 K/s [18]. Due to the space limitations on the press, as well as coupon geometry, it was necessary to employ alternative quenching methodologies that would produce a comparable final microstructure. The two main methods used in this work were oil and a forced air quenching apparatus.

4.2.1 Oil Bath Quenching

Oil was initially chosen as the quenching medium for heat treated blanks, as it produces as relatively low quenching rates (on the order of 250 K/s [13]). This quenching rate is more than sufficient to develop a fully martensitic microstructure, assuming full austenitization occurs during the testing. Unfortunately, oil has a tendency to deposit hydrocarbons on the surface of the coupons. While this does not affect the microstructure, it does affect the surface finish, making it difficult to observe any macroscopic changes undergone as the Al-Si coating transforms into the Al-Si-Fe intermetallic layer.

To combat this, a water bath was tested. Water results in a much higher quenching rate (approximately 2200 K/s [13]), and was found to impart residual stresses within the coupons during quenching, resulting in significant deformation. Stress-induced deformation would make any results elicited from tensile testing inaccurate due to the need to straighten the specimens before actually deforming them, however for the purposes of examining the development of the Al-Si coating, water is an acceptable quench medium.

4.2.2 Forced Air Quenching Apparatus

As an alternative, a forced air quenching apparatus (FAQA), seen in Figure 19, was used. This device was originally developed by Bardelcik et al. [45], and allows for average quenching rates of 14, 17, 24, 28, and 50 K/s, depending on its configuration. The FAQA consists of a series of adjustable air blades connected to a compressed air manifold. The racks upon which the air blades are mounted can be adjusted at 25 mm intervals, with the shortest distance being

75 mm from the coupon. The coupon is held in a vertical position with ceramic inserts, allowing the compressed air to impinge upon both surfaces simultaneously, ensuring an even quench. The heated coupons are placed manually in the support inserts using tongs.

For these experiments, the narrowest set point (75 mm from the coupon), correlating to a quenching rate of 50 K/s, was used. This was done to ensure that a fully martensitic crystal structure was formed; while 28 K/s would also have developed a fully hardened structure, it is very close to the critical quenching rate, and any slight variations in the compressed air pressure or flow rate could drop the quenching rate below critical, thus changing the outcome of the experiment. In comparison to the in-die quenching, cooling rates experienced by the blanks range between 75 and 225 K/s, depending on the instantaneous relative temperatures of the quenching die and the blank [40].

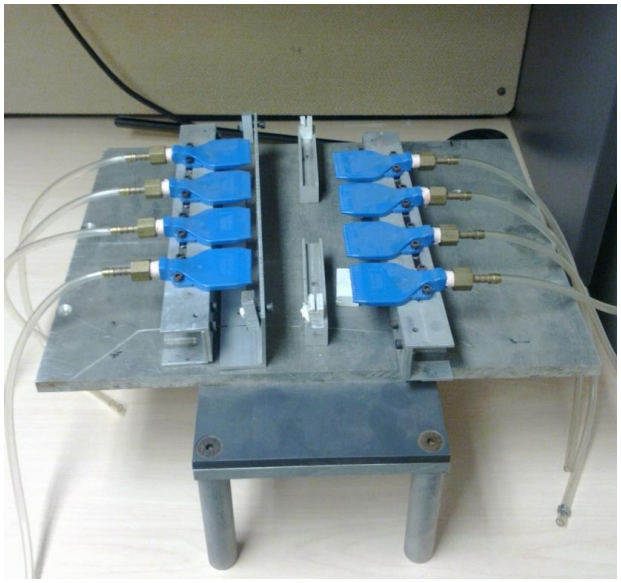

Figure 19 - Forced air quenching apparatus (FAQA) used for simulated die quenching.

4.3 Control and Monitoring

4.3.1 Hydraulic Press Control

The hydraulic press used for testing was the 250 ton Macrodyne® press in the High Pressure Lab. The press was directly controlled with an MTS FlexTest® SE controller, which allows for

the ram to be controlled by displacement and by applied load. The press was initially controlled manually through the FlexTest® system by adjusting the position of the ram based on its relative displacement from a predefined zero location. The ram was opened and closed by the operator after coupons were loaded into the die. This methodology caused a large variation in applied load to the coupon by the ram, which resulted in the expulsion of the liquefied Al-Si coating from between the coupon and the striking surfaces at higher pressures.

Because this method is inconsistent and unstandardized, it produced unrepeatable experimental results. Consequently, a LabVIEW program was developed to control the relative displacement (and, effectively, the applied load) of the ram during the heat-up, heat treatment, and cool-down phases of the monolith's operation. Displacement set points were identified manually in order minimize the applied load experienced by the coupons. These set points were then used by the LabVIEW software to ensure the ram moved into the correct position at the appropriate time during testing.

4.3.2 Temperature Control

The temperature within the monolith was measured by K-type thermocouples (at locations C and E as seen in Figure 8) that provided data to two PID temperature controllers. The controllers would switch the electrical current provided to the heating elements on and off based off of the pre-programmed set-point temperature, using a hysteresis (or "bang-bang") control algorithm [46]. The set points for the PID controllers used were inputted manually and individually; they were not used for recording internal temperatures.

4.3.3 Current and Temperature Monitoring

Additionally, the LabVIEW program was designed to monitor and record the electrical current passing through each element bank in real time, the temperature of three locations within the monolith, and a fourth temperature measurement to capture the heating rate of instrumented coupons. The data captured by the program was then used to improve the accuracy of the COMSOL models, and to ensure that the coupons reached the desired temperature in an acceptable timeframe. When monitoring the temperature of the coupons, the program would

also automatically open the press when the desired temperature threshold had been reached. The coupon temperature measurements were also fed into the Gleeble® 3500 thermomechanical simulator to perform a dilatometric analysis to verify full austenitization within the specimen.

4.4 Testing Procedure

During testing, one person controlled the LabVIEW software, ensuring that the correct program path was being executed during the testing phase. This person was responsible for opening and closing the monolith while the coupons were loaded and removed. The second person, wearing appropriate personal protective equipment (including Kevlar gloves, a reflective heat shielding jacket, and a face shield), would load the coupons into the monolith using tongs, and would indicate to the computer operator when it was safe to initiate the next phase of the program. Un-instrumented coupons were heated for pre-determined times, generally 20, 25, or 30 seconds. The computer operator manually initiated the program to open the monolith at the end of the time, allowing the second person to remove the coupon from the die with tongs, and quench it using the FAQA or an oil bath. After the heat-treatment, the coupons were labeled with a code that indicated the specimen number, specimen rolling direction, die surface temperature at loading, heat treatment time, and quenching medium.

4.5 Furnace Heat Treatment

For comparison with those processed through direct contact heating, a series of coupons used as a "control" group were heated in a furnace held at 950°C for seven minutes, mimicking traditional furnace heat treatments used in the majority of existing HFDQ processes, and then quenched in oil. As noted above, oil quenching provides a quenching rate comparable to the rate achieved in typical die quenching.

4.6 Post-Heat-Treatment Experimentation

Three tensile samples and five cross-sectional samples were created from each processed coupon to characterize the final tensile strength and hardness. Figure 20 shows the sample map of where each specimen was taken. The five microhardness cross-sections were held together

with a binder clip before being hot-mounted in a Bakelite puck. The samples were then ground using sandpapers of increasing grit (beginning at 220 and ending at 1200), followed by polishing with a 3 µm diamond suspension and 1 µm colloidal silica suspension. The samples were then etched with a 3% nital solution in order to reveal the microstructure of the each sample.

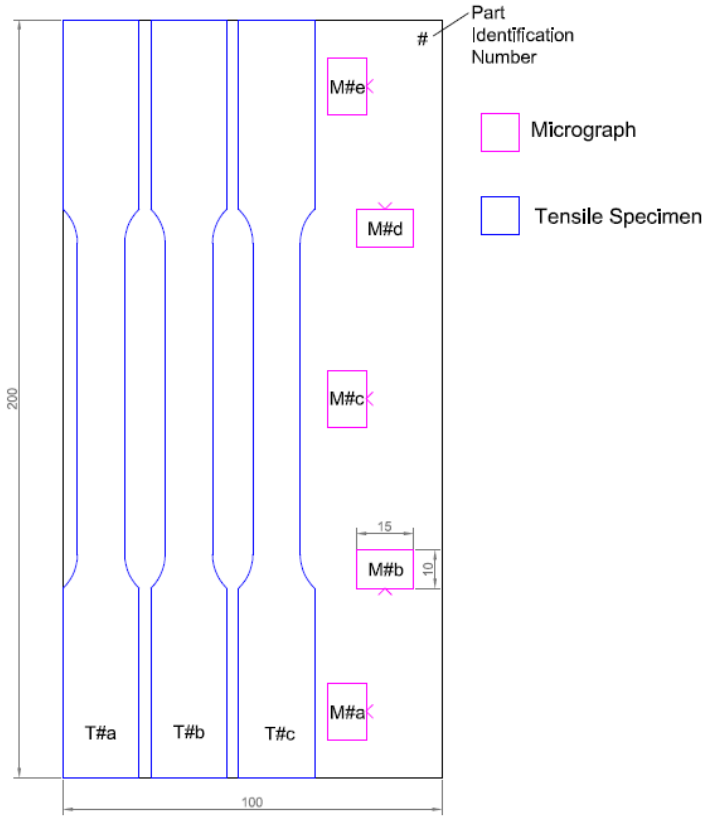

Figure 20 - Layout of the blank that shows where samples were taken. Arrows on the micrograph samples indicate the faces to be studied.

Three microhardness indentations were made on each of the five cross-section micrograph specimens. Microstructures with hardness measurements greater than 450 HV were assumed to have a fully martensitic microstructure, following [8]. The microhardness locations are shown in Figure 21.

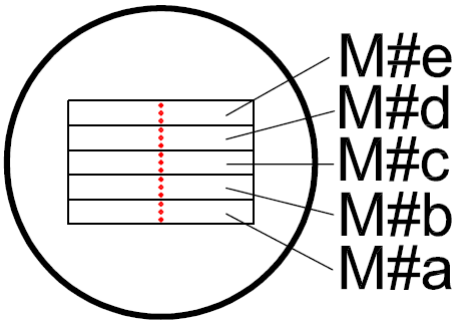

Figure 21 - Specimens and locations for microhardness testing.

Micro-hardness measurements were made using a LECO MHT Series 2000 hardness tester with a 500 g load. The hardness value is calculated by indenting the surface of a specimen with a set force using a diamond indenter and measuring the size of the indentation under a microscope using Equation (11). An indentation sample is shown in Figure 22.

$$HV = \frac{2F\sin(136^{\circ}/2)}{d^2} \tag{11}$$

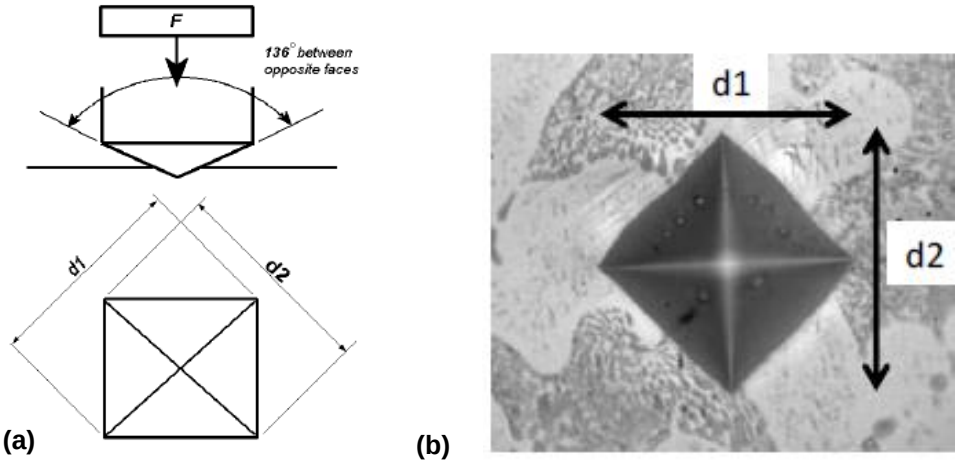

Figure 22 - Microhardness testing apparatus (a) indenter, and b) a sample indentation shown in an optical micrograph [47].

Three tensile specimens were taken from each sample in order to ensure consistency in the results. The tensile specimens were machined to ASTM E8 standards for a sheet specimen, as

outlined in Figure 23 and Table 2 [48], and were pulled at 0.02 mm/s. Care was taken to avoid heating the samples excessively during machining to prevent any further changes in microstructure.

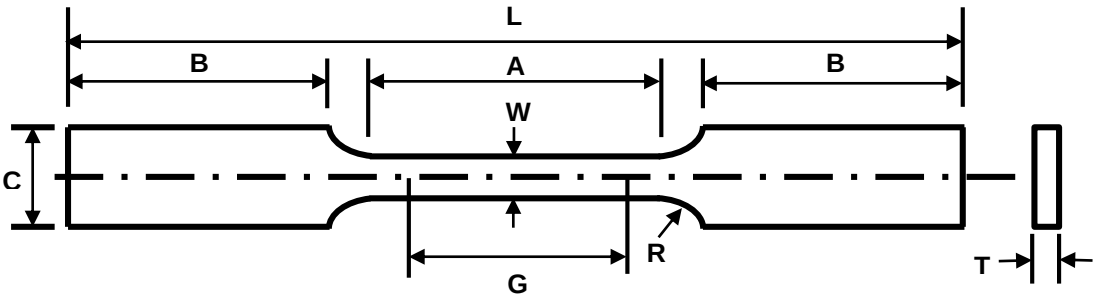

Figure 23 - Dimensions of tensile specimens as per ASTM E8 [48].

Table 2 - ASTM E8 standard dimensions for a dog-bone tensile specimen [48].

Measurement	Sheet-Type, 12.5 mm Wide
	mm
G – Gage length	50 ±0.1
W – Width	12.5 ±0.2
T - Thickness	Thickness of material
R – Radius of fillet, min.	12.5
L – Overall length, min.	200
A – Length of reduced section, min.	57
B – Length of grip section, min.	50
C – Width of grip section, approx.	20

Chapter 5
Results, Validation, and Discussion

Using the heated monolith design presented in Chapter 3, and the testing methodologies discussed in Chapter 4, Chapter 5 presents the experimental results elicited from testing. The measured operating parameters are presented, and the numerical models presented earlier are revised and validated. Experimental results verifying homogeneous austenitization under the given process parameters are shown. The development of the Al-Si-Fe intermetallic coating in both homogeneous and tailored heating regimes are analyzed and discussed.

5.1 Monolith Operation

In the first iteration of experimentation, the heated monolith was brought to its target temperature of 1000 °C in four 250 °C steps, and held for approximately 60 minutes at each step to allow the monolith to reach thermal equilibrium. This was done to ensure smooth operation, and to protect the fragile heating elements from any excess strain caused by unanticipated thermal expansion within the monolith.

When it was found that the monolith could be brought to temperature in gradual steps, it was necessary to determine the maximum ramp-rate by setting the PID controllers to 1000 °C, and monitoring the heating time. The monolith was able to reach its target operating temperature in approximately 47 minutes, as can be seen in Figure 24. This is promising from an industrial standpoint, as a fully automated system would be able to turn on and ramp to temperature in advance of the commencement of production in a relatively short period of time. This would allow the user to shut off the power to conserve energy at the end of the preceding shift, and turn it on and have it at temperature the next morning. Comparatively, roller hearth furnaces are often kept at temperature for several months at a time due to the required time and power required to shut down and re-heat the equipment.

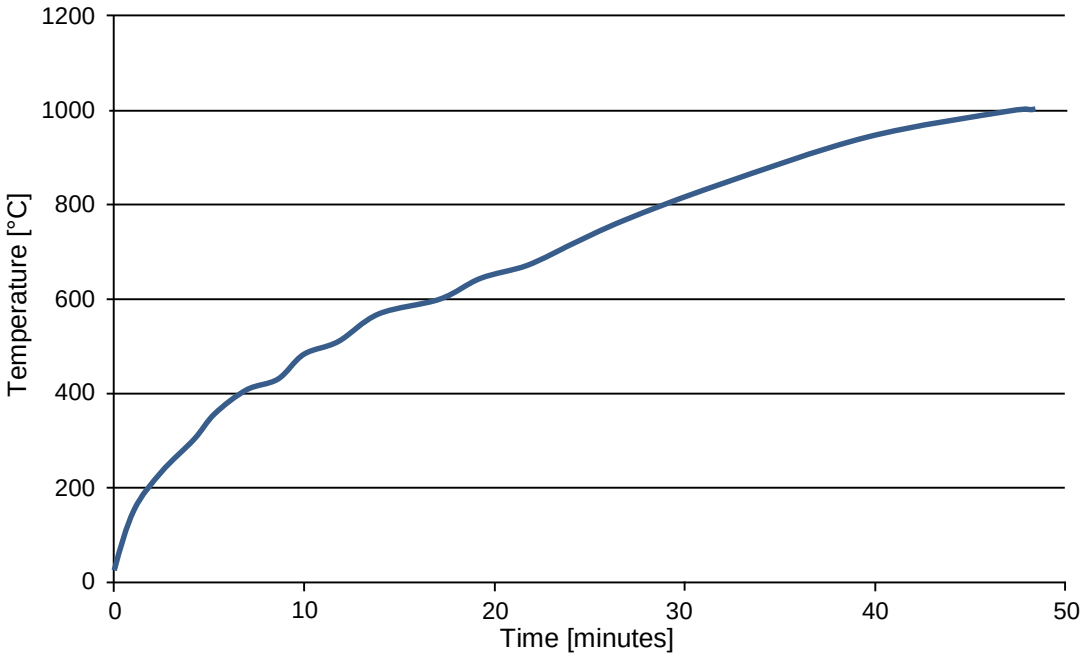

Figure 24 - Measured maximum ramp rate for heated monolith.

As testing proceeded, however, it was found that heating the monolith at its maximum ramp rate could cause the SiC heating elements to fracture. Further investigation revealed that repeated rapid heating and slow cooling of the monolith would cause the alumina inserts used for electrical isolation to crack and crumble, and become lodged in between the heating element and the wall of the borehole. These shards would cause point loads in excess of recommended limits to be applied to the brittle elements, causing them to fracture, as seen in Figure 25. This issue was alleviated by increasing the diameter of the boreholes to allow for more lateral movement, and by step-wise heating to ensure homogeneous temperature distribution within the monolith. The step-wise method allowed for a smaller degree of local thermal expansion within the monolith, thus ensuring that the alumina inserts and elements would be subject to fewer stresses.

Figure 25 - Fractured heating element caused by the application of stress during non-uniform thermal expansion of the monolith.

5.2 Monolith Heating Model Validation

Initial testing showed that the FEM-predicted monolith temperatures exceeded measured values by approximately 100 K, so the FEM simulation was repeated using the measured current supplied to the heaters to calculate the heat flux boundary condition on the inner surface of the monolith boreholes, based on the specified electrical resistance of the SiC elements (rated at 1.57 ohms, ± 20%.) Accordingly, three scenarios were considered in the revised model: heat fluxes were calculated using the upper bound, lower bound, and nominal power dissipation of the heating elements. Figure 26 shows the predicted and measured temperature profiles for thermocouples D and F. The plots indicate that using the lower bound of the elements' resistivity results in modeled temperature profiles that more closely follow the experimental measurements.

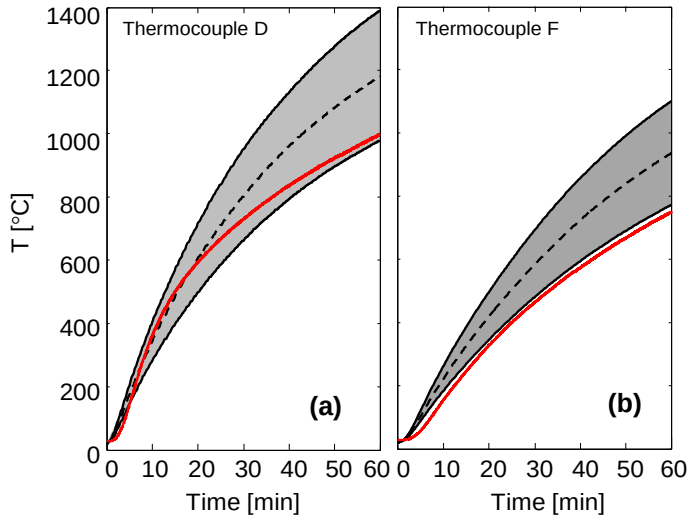

Figure 26 - Upper and lower bound of predicted thermocouple temperatures, compared to measured temperatures for (a) thermocouple D and (b) thermocouple F.

5.3 Verification of Austenitization

To gain further insight into the austenitic transformation, a dilatometric analysis was performed using a C-gauge dilatometer in a Gleeble® 3500 thermomechanical simulator. Usibor® 1500P "dog-bone" coupons with a gauge length of 25.4 mm and a gauge width of 6.35 mm were used. The coupons were electrical resistance heated according to a programmed temperature history; the coupon temperature was controlled by a K-type thermocouple welded on the center of the sample. The temperature variation across the gauge width was within 1°C for a thermocouple reading of 1000°C.

Two samples were heated according to the direct contact heating profile shown in Figure 27, while another two samples were held at the peak temperature for additional 3.9 seconds (total processing time of 25 seconds). The dilatometric curves of all four tests show an excellent consistency; an example is plotted in Figure 28. The critical temperatures T_{Ac1} (starting temperature of austenite formation), and T_{Ac3} (finishing temperature of austenite formation) are indicated in the figure. Prior to the Ac1 temperature, the dilatometric curve increases linearly, as the ferritic microstructure experiences uniform temperature-dependent thermal expansion. Beyond the Ac1 temperature, the dilatometric curve indicates a contraction in the

specimen; this phenomena is due to the transformation of the ferrite to austenite [49]. Beyond the Ac3 temperature, the curve once again begins to increase linearly with temperature. This indicates that the microstructure has fully austenitized, and that the austenite grains are increasing in size due to thermal expansion [49]. In contrast, the research completed by Ploshikhin et al. [50] found that 40 s was sufficient to austenitize the coupons at temperatures between 920 °C and 940 °C, however the longer duration compared with our test is likely due to a lower rate of thermally activated austenitization as the temperature decreased.

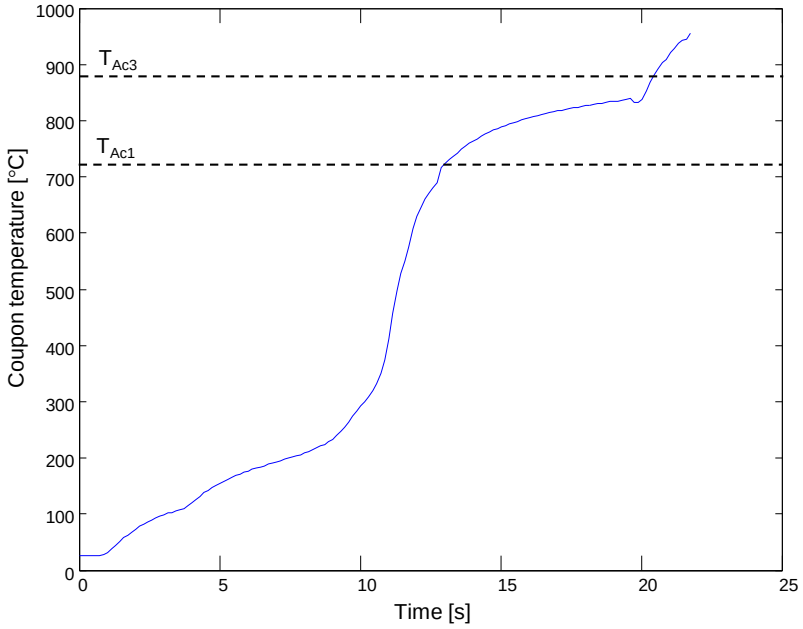

Figure 27 - Measured temperature history of a coupon heated via direct contact.

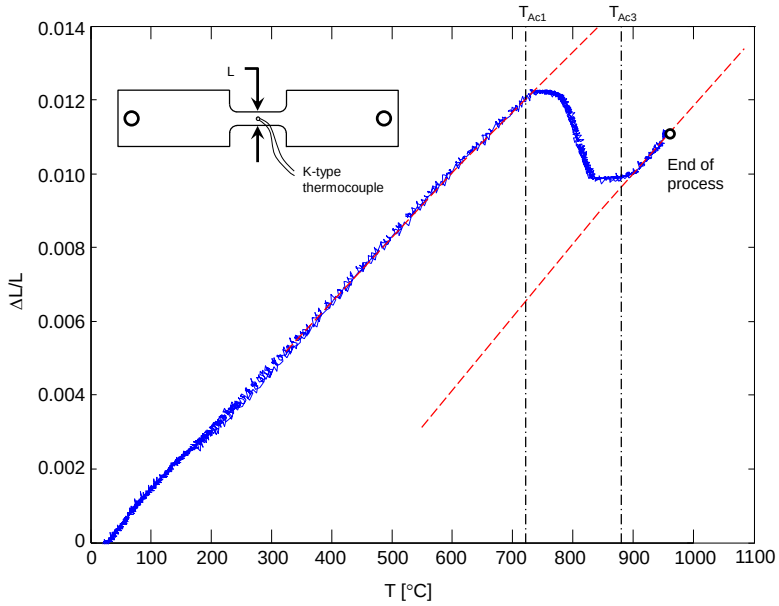

Figure 28 - An example dilatometric curve obtained by heating a dog-bone coupon according to an experimentally-derived heating schedule.

5.4 Direct Contact Heating Results

Figure 29 shows the microstructural evolution of the samples after the direct contact heating and furnace heating. The microstructure of the as-received Usibor® 1500 P steel is composed of ferrite and pearlite with the grains orientated along the rolling direction. Uniform martensitic microstructures with parallel lath crystals are observed in both heated samples, suggesting that the coupons are able to at least be partially transformed into austenite by the direct contact and furnace heating methods. The direct contact heated sample displays a finer lath structure relative to that of the furnace-heated one, likely due to the limited time available for the austenite grains to grow within the relatively short duration of direct contact heating.

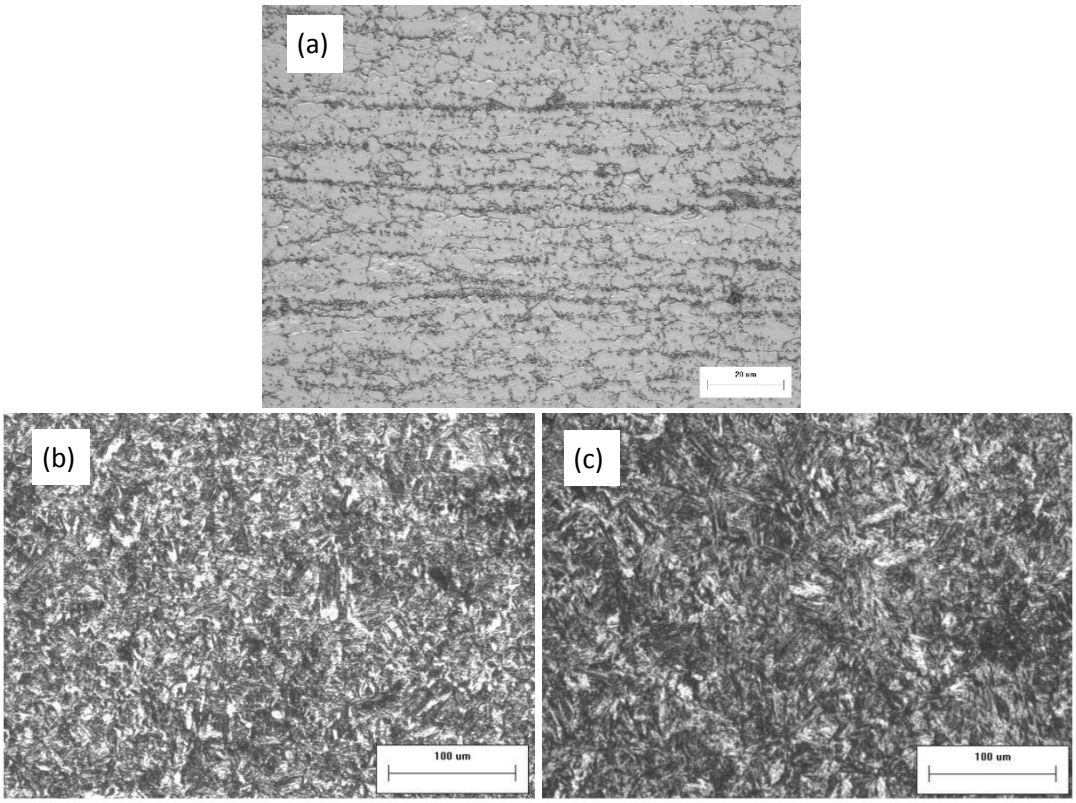

Figure 29 - Optical micrographs showing the microstructure of (a) the as-received coupon, (b) a direct-contact heated and (c) a furnace heated coupon, after oil quenching.

Tensile tests were conducted on six tensile specimens cut from the as-received coupons, as well as twelve heat-treated tensile specimens, six of which were cut from coupons treated via direct contact heating, and six from furnace heating. The average value for each specimen type can be found in Figure 30, and the maximum, minimum and average ultimate tensile strength (UTS) can be found in Table 3. The as-received sample shows an ultimate tensile strength at about 500 MPa and a total elongation of 27% prior to fracture. On the other hand, the ultimate tensile strengths of both direct-contact/quenched and furnace heated/quenched samples is significantly larger at approximately 1500MPa, which is consistent with the tensile strengths of hot stamped 22MnB5 steels reported in the literature [51, 52]. This suggests austenite has been completely transformed during heating, resulting in a full martensitic

transformation after quenching, which is consistent with the microstructural observations in Figure 29 b and c.

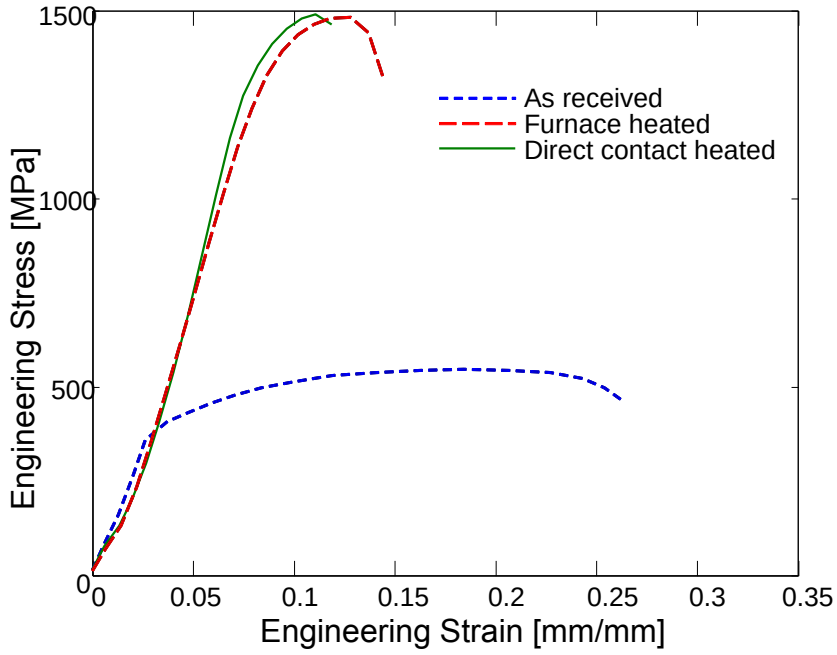

Figure 30 - Average stress versus strain curves for as-received, direct contact heated/quenched, and furnace heated/quenched Usibor® 1500P coupons.

Table 3 - Maximum, minimum, and average UTS for each specimen type.

Specimen	Ultimate Tensile Strength [MPa]		
	Maximum	Average	Minimum
As-Received	544	533	526
Direct Contact Heated	1514	1478	1437
Furnace Heated	1486	1469	1455

The average measured Vickers micro-hardness for two of the direct contact heated and two of the furnace heated samples after oil quenching are presented in Table 4. The former shows a slightly higher hardness value, around 500 HV, relative to the latter with an average hardness value of 481 HV. This is likely correlated with the refinement of martensite grains in the direct contact heated sample (Figure 29), resulting in an increase in the material hardness. Moreover,

compared with the furnace heated sample, the measured hardness distribution through the thicknesses of the direct contact heated samples was relatively constant with lower deviation of the measurements.

Table 4 - Vickers micro-hardness of direct contact heated and furnace heated samples after oil quenching.

Measurement	Process			
	Direct Contact 1	Direct Contact 2	Furnace 1	Furnace 2
Average	491 HV	504 HV	476 HV	487 HV
Std. Deviation	6.35	13.79	20.65	37.57

5.5 Phase Transformations in the Al-Si Coating

The aluminide layer of the as-received sample is composed of an Al-Si top coating and an inner continuous intermetallic layer with an average total thickness of 28 µm (Figure 31a). The intermetallic phases were reported to be Al_7Fe_2Si and Al_5Fe_2 [53]. The Al-Si coating completely transformed into an Al-Si-Fe intermetallic layer with an increasing thickness of 32 µm after the direct contact heating, as observed in Fig. 11b. The cross-sectional microstructure was further examined using the FE-SEM, and the chemical composition of the intermetallic phases were identified by EDS, as shown in Fig. 12 and Table 3.

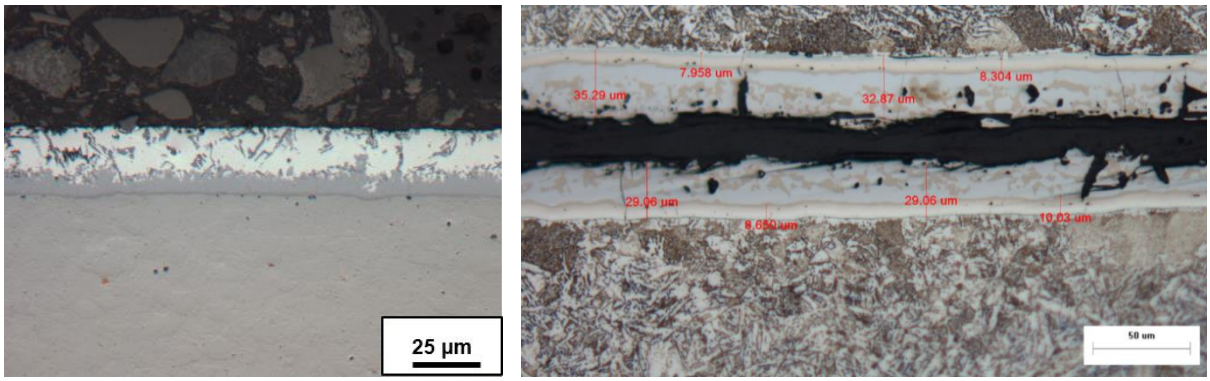

Figure 31 - Micrograph showing (a) the as-received structure and surface coating, and (b) the fully-formed Al-Si-Fe coating on a direct contact heated Usibor® 1500P coupon that was quenched in oil.

The formed Al-Fe-Si intermetallic layer consists of three types of sub-layers (Figure 31b and Figure 32, Table 5). The top sub-layer is comprised of Al_5Fe_2 and AlFe intermetallic phases. The Al_5Fe_2 phase forms during initial heating, as a result of diffusion of iron from the 22MnB5 steel substrate into the molten Al-Si coating [42, 54]. Subsequently, the Al_5Fe_2 phase transforms into AlFe due to iron diffusion and enrichment of iron at the coating and steel interface [42, 54]. Another sub-layer adjacent to the steel substrate was verified to be α-Fe (indicated above the dashed line in Figure 32), which forms when the aluminum and silicon diffuses into the steel substrate and stabilizes the BCC iron lattice [54, 55]. A thin sub-layer between the Al_5Fe_2 and AlFe intermetallic layer and the α-Fe layer is also identified as AlFe phase. Kirkendall pores were observed within the α-Fe layer, due to a higher diffusion rate of aluminum into the steel substrate compared to iron diffusion into the coating [54]. The intermetallic phases formed in the direct contact hearing process are consistent with those reported during a furnace-heating prior to the HFDQ process [42, 54].

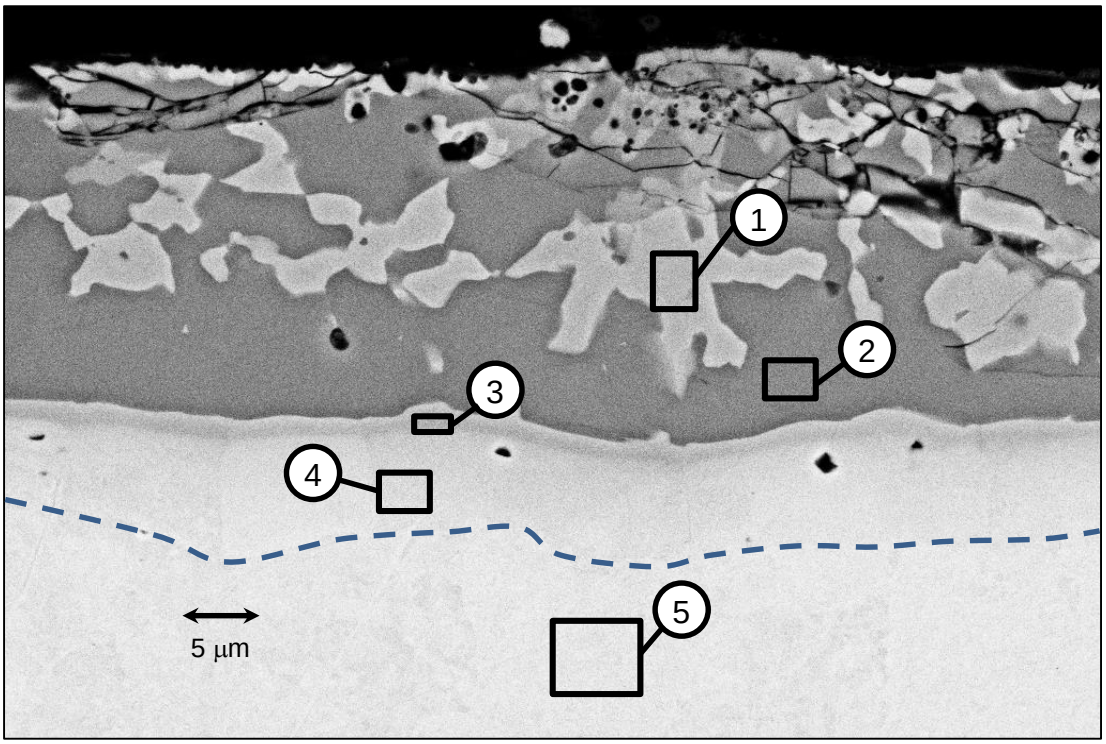

Figure 32 - SEM image of the cross section of a 25-second direct-contact heated Usibor® coupon, with EDS investigation regions highlighted. The dotted line denotes the separation of the α-Fe region from the steel substrate.

Table 5 - Chemical composition of Al-Si-Fe intermetallic phases by EDS.

Num.	Phase	Chemical Composition (at.%)			
		Al	Fe	Si	Mn
1	AlFe	39.59	41.82	17.52	1.07
2	Al_5Fe_2	70.57	27.05	1.86	0.51
3	AlFe	39.67	43.47	13.88	0.96
4	α-Fe	14.77	79.09	4.44	1.20
5	Fe substrate	0.45	92.91	0.59	1.72

In comparison to the work of Ploshikhin et al. [50], the samples treated at a higher temperature and for a shorter period of time in present study developed a more distinct lamellar structure, with a clear diffusion path visible in both optical and scanning electron microscopy. Additionally, the results of this work reveal that a distinct α-Fe diffusion layer with a thickness of approximately 8 μm was fully developed, whereas the formation of α-Fe layer was not

clearly observed during the contact heating at lower temperatures reported by Ploshikhin et al. [50]. The brittle Al_5Fe_2 phase in the aluminide layer is prone to crack and leads to the interfacial debonding of the coating during subsequent hot forming operations [56]. However, the presence of α-Fe layer aids in preventing the propagation of micro-cracks to the steel substrate, thus maintaining the integrity of the coating with the steel sheets [56].

5.6 Striking Surface Fouling Prevention

After testing each of the interchangeable surfaces, it was found that the Amdry®/Metco® combined coating produced the best results. The high-polish surface drastically increased the degree of adhesion and fouling that occurred, and was rejected very quickly. The boron nitride aerosol coating did help reduce adhesion, however the coating degraded after only a few cycles. Once the integrity of the coating was compromised, adhesion would once again begin. While this could potentially work on a very low throughput operation, it would not be feasible to use it on an industrial scale. The three plasma vapor deposited coatings each reduced the adhesion of the coupons to the surface, however the Metco® Diamalloy® coating caused Al-Si coating to be deposited on the striking surface. This suggests that it could quickly become fouled in an industrial setting, potentially increasing operating costs an unreasonable amount. Both the Metco® 410 and Amdry®/Metco® combined coating did not appear fouled after several tests, however, the combined coating produced a superior surface coating texture; the Metco® 410 coating left the Al-Si layer very rough and pockmarked, which may ultimately lead to welding and paint issues in latter stages of production.

It should be noted that several tests were performed with coupons coated in boron nitride to see if the adhesion issue could be mitigated, and results were promising. However, further study is required to see if the coating would interfere with welding, if it could be completely removed with existing cleaning operations, and, if cleaning is not entirely successful, what effect it would have on painting processes.

Chapter 6
Tailoring Material Properties

One of the advantages of utilizing a direct contact heating approach is possibility of tailoring material properties through manipulation of heating rates. From the success of the approach presented in Chapter 5, this chapter shall detail the development of a proof-of-concept direct contact heating monolith for the tailoring of material properties.

6.1 Material Selection and Striking Surface Design

In order to test the feasibility of tailoring the crystallographic properties of the heat-treated coupons, a striking surface was designed to produce two markedly different heating rates despite being at the same temperature. This tailoring plate consisted of an RA330® matrix with embedded RSLE 57® sections, shown in Figure 33. This design exploits the fact that for the specific case of semi-infinite slabs, as explained in Section 3.2.1, the heat transfer rate between the striking surface and the coupon is dependent on the thermal effusivity, $e = \sqrt{k\rho c_p}$, of the striking surface [35]. This allows for drastically different heating rates, even if the striking surface is at a uniform temperature.

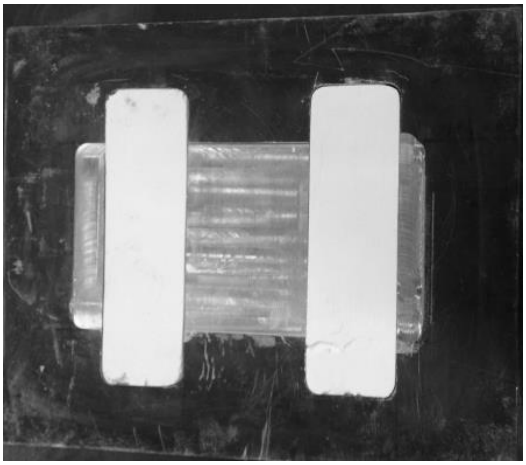

Figure 33 - Striking surface for tailoring, composed of RA 330® (light grey and black) inlayed with RSLE 57®.

A 1D heat transfer model was constructed using the same methodology presented in Chapter 3, and was used to estimate the anticipated heating times to achieve a fully austenitic crystal structure within a coupon in contact with either RA330® or RSLE57®. The thermophysical properties of these materials are summarized in Table 6.

Table 6 - Thermophysical properties of RA330® and RSLE 57® [39, 57].

	k [W/(m·K)]	ρ [kg/m^3]	c_p [J/(kg·K)]	e [J/(m^{2}Ks$^{1/2}$)]
RA330®	25.4	7944	576	10784
RSLE 57®	0.75	2100	705	1054

Assuming that both materials are at uniform 1000°C, the model predicts that the RA330® areas would be able to heat the coupons to 950°C in 21 s, whereas the RSLE 57® areas would require 365 s to achieve full austenitization. A comparison of the predicted heating times can be seen in Figure 34.

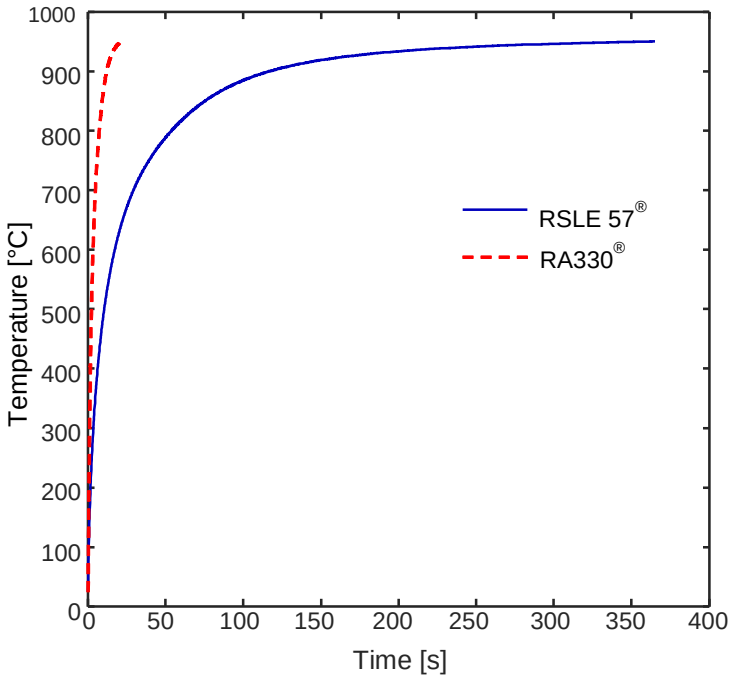

Figure 34 - Simulated blank temperatures obtained using a 1D heat transfer model and the thermophysical properties presented in Table 6.

While this model is provides valuable information for theoretical heating rates when in contact with *exclusively* RA330® or RSLE 57® for design purposes, it is inherently inaccurate since a 1D model cannot predict conduction occurring in a real 3D blank. Referring to the heating rates observed in Figure 34, if 1D conduction is assumed to be accurate, at the 20 second mark, the region of the coupon in contact with the RA330® will be around 400°C hotter than the sections in contact with the RSLE 57®, and clearly there would be considerable heat conduction tangential to the interface that is not captured by the 1D model.

To correct for this, a 3D heat transfer model was made in COMSOL to predict the heating times required for the blank. The model was simplified to only consider the lower striking surface, Usibor® coupon, and the upper striking surface; this was done to reduce the net computational load. This model utilized the simulated temperature data from the COMSOL model for the entire monolith heated for 60 minutes as the initial temperature condition for both striking surfaces. The edges of the striking surfaces were modelled as perfect insulators, as it is assumed at because of the power input to the die, the heat loss over the course of heating will be minimal. The Usibor® coupon was defined as being at room temperature. A grid-refinement study showed that the predicted temperature became grid-independent with 6579 elements. The predicted temperature distribution within a coupon heated for 60 s can be seen in Figure 35.

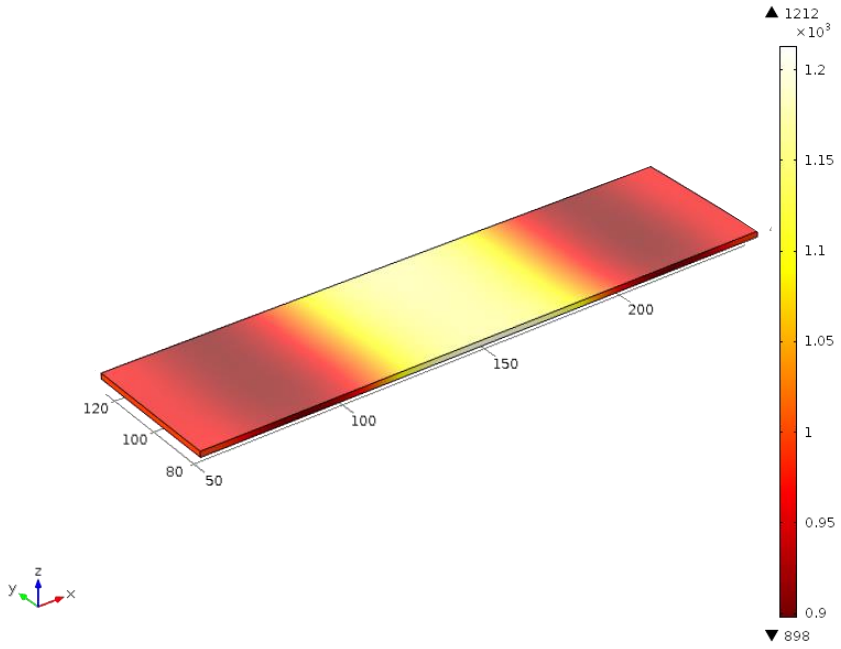

Figure 35 - Predicted temperature distribution within the coupon; temperature in K.

This study showed that, for the given geometry of the coupons, a heating time of 25 seconds (which should otherwise be sufficient for non-tailored direct contact heating) would be insufficient to bring the zone in contact with the RA330® to the austenitization threshold. As expected, the temperature gradient induced a sufficient amount of axial heat conduction to lower the temperature of the region in contact with the RA330®. While this issue is apparent for this scale of testing apparatus (the slow heating rate regions account for slightly less than 50% of the total coupon area), it is predicted that for an industrial-scale prototype using substantially larger coupons, the axial conduction effect will be less pronounced on the cross sectional temperature. This is due to the fact that the region in contact with the RA330® will account for a far higher percentage of the total surface area, and, as such, will have much more thermal inertia, thus minimizing the conduction effect.

6.2 Sample Preparation and Process Variation for Tailoring

While the coupons tested in the homogenous case were measured by one thermocouple, the nature of tailoring surface lent itself to measurement by three thermocouples: two along the

centerline of the RSLE 57® sections, and one along the center of the central RA330® region, as seen in Figure 37.

The experimental tailoring procedure was essentially the same as the general direct contact procedure described in Section 4.4, however in order to ensure that the coupons were in proper contact and alignment with the tailoring pattern, the person loading the coupon had to ensure the coupon followed a slim guiding bezel machined into the striking surface. Once the coupon was in position, the procedure continued in the same manner described previously.

6.3 Post-Processing for Tailored Samples

For the tailored samples, 75-mm-long, 2-mm-thick samples were selected from the "transition region" shown in Figure 33. These samples were cold mounted in an epoxy resin in groups of four, as can be seen in Figure 36. Micro-hardness measurements were made using a LECO MHT Series 2000 hardness tester with a 500 g load. Twenty-eight microhardness measurement locations, spaced 2.54 mm apart, were used in each sample to measure the hardness. At each location, the hardness is measured three times in order to ensure consistency across the thickness of the specimen.

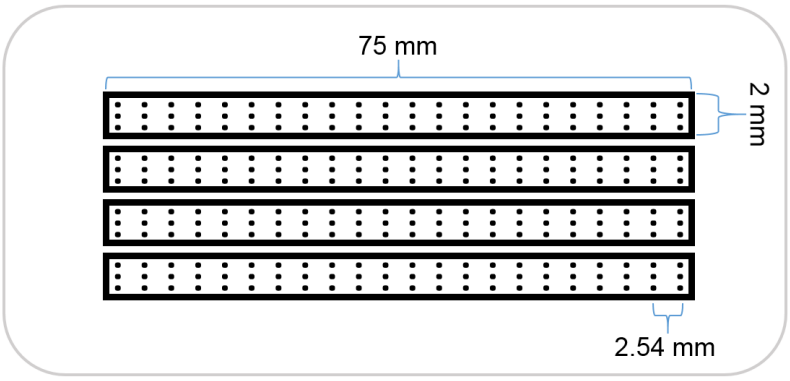

Figure 36 - Hardness measurement map for tailored samples.

6.4 Results of Tailored Austenitization Tests

6.4.1 Temperature Measurements and Model Validation

A coupon with three embedded thermocouples was used to determine the actual heating rates experienced in the blank regions in direct contact with the RA330® and RSLE 57®. Three 1 mm deep channels were machined out of four coupons, aligned with the midlines of the insulated and uninsulated zones of the striking surface. These channels were then instrumented with K-type thermocouples, following the same methodology described in Section 4.1.1. The monolith was heated to its operating temperature, and the instrumented coupons were inserted into the apparatus following the procedure described in the previous section.

The coupon temperatures in Figure 37 show that the regions contacting the RSLE 57® (TC_1 and TC_3) experience appreciably lower heating rates compared to TC_2, which contacted the RA330®. The heating rates are similar to those predicted by the 3D COMSOL model, however it can be seen in Figure 37 that there is initially a slower heating rate experience by the coupon while it is loaded into the die, and the press moves to the closed position. Because this period was not captured by the model, several temperature discrepancies presented themselves. To correct for this, the coupon initial temperature condition was raised from room temperature to 220 °C (the measured temperature just as the upper die closes and the heating rate increases markedly). This change greatly improved the agreement between the model and the experimental data, as seen in Figure 38.

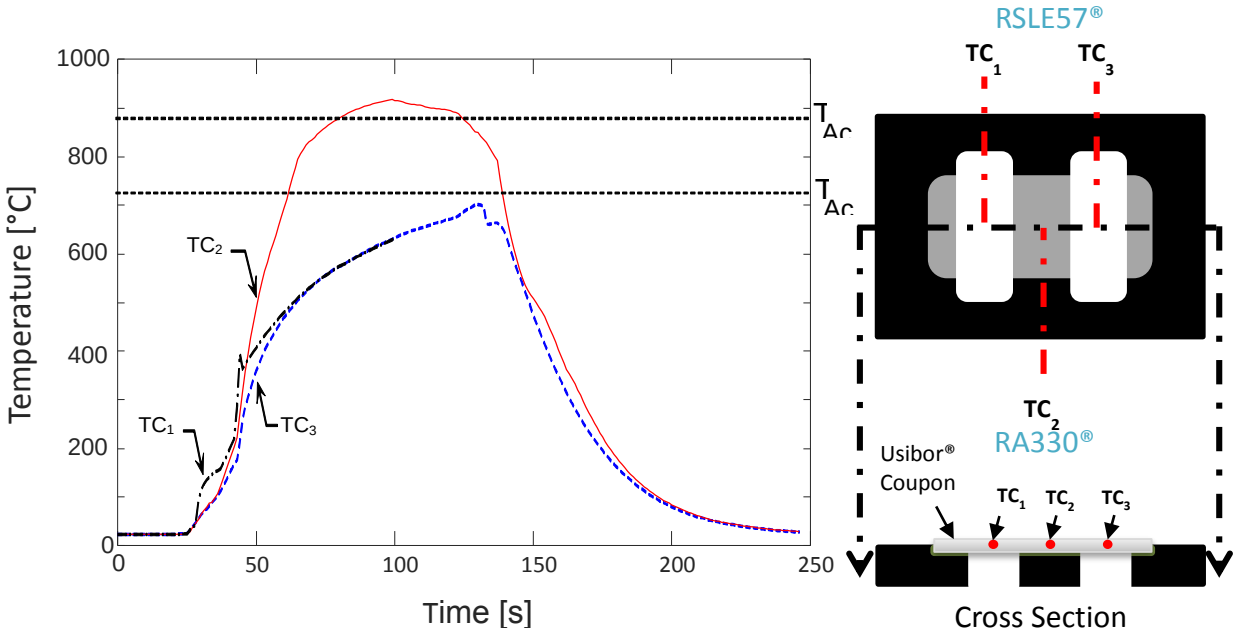

Figure 37 - Usibor® coupon temperature histories at thermocouple locations indicated.

As a consequence of axial conduction through the coupon, more time is needed for high-temperature regions of the coupon to fully-austenitize compared to homogeneous direct contact heating. The experiments described in the previous section achieved complete austenitization in approximately 21 seconds with a striking surface of solid RA330®, while the central region required nearly 60 seconds to reach a temperature of 915°C using the composite RA330®/RSLE 57® striking surface. This effect is quite pronounced in the present experiment due to the comparatively small (<50%) region of the coupon that is in contact with the RA330®, in which case the axial conduction to the cooler areas of the coupon strongly limits the peak temperature in the coupon at any instant. We hypothesize that the time to austenitize would be significantly reduced if the ratio of RA330® to RSLE 57® contact area were increased.

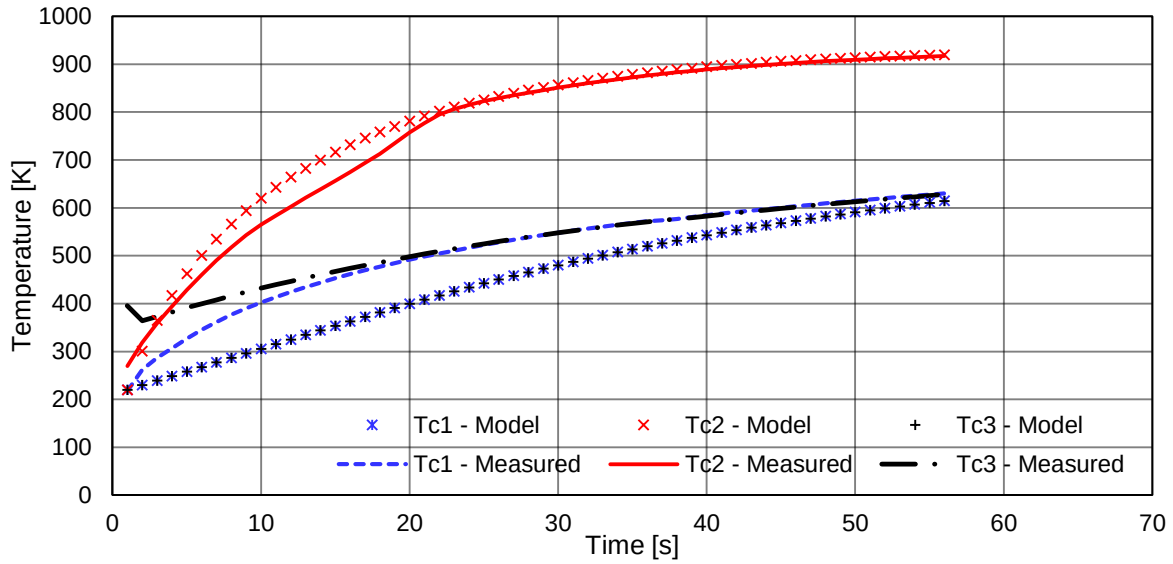

Figure 38 - Measured versus modelled temperatures within a tailored coupon.

6.4.2 Microhardness Map and Analysis

Subsequent tests were carried out on coupons heated for 20-180 seconds within the monolith and then air-quenched using an apparatus that simulates blank cooling rates during forming [45]. As mentioned previously, segments were taken from the centerline of each heat treated specimen, extending from the middle of the uninsulated region to the middle of the insulated region, cold-mounted in an epoxy resin, ground and polished for microhardness analysis, and further etched in a 5% nital solution for optical microscopy.

Microhardness measurements, calculated from the average of the three indentations at each sample location (see Figure 36), for 180, 90, 60, and 20 seconds, are plotted in Figure 39. The three microhardness values measured at each sample location were found to be within 10% of each other, at most, with an average variance of approximately 5%. The axial heat conduction effect is particularly pronounced in the hardness profile obtained from 90 seconds of heating. The increase and decrease in hardness over the first 15 measurement locations indicates that heat was conducted through the part to the insulated regions, as the whole central region was unable to achieve a fully austenitic (and, therefore, a fully martensitic) structure. It should be noted the measurement locations for the 90 s sample are likely not properly aligned with the

other samples; due to the manual method of loading and unloading coupons from the monolith, a small misalignment of the coupon with the die could appreciably offset the results. Comparatively, the 180 s heat treatment shows that the part was able to achieve a fully martensitic structure in the uninsulated region, and achieved a softer and more ductile structure in the insulated region. Moreover, the transition from martensite to the ductile phase occurred over a span of 6 mm.

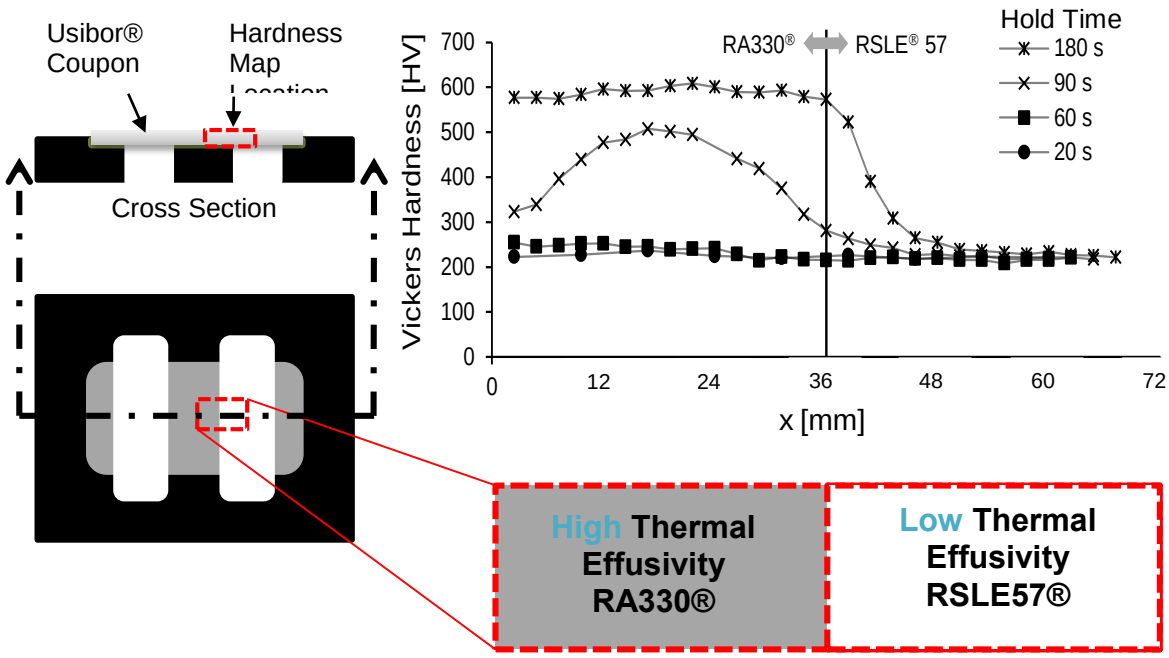

Figure 39 - Location and results of Vickers hardness mapping for tailored Usibor® 1500P coupons at various hold times.

6.4.3 Scanning Electron Microscopy

To observe the extent of the transformation of the Al-Si coating, an energy-dispersive x-ray spectroscopy (EDS) investigation was performed on the 180 second sample using one of WATLab's scanning electron microscopes (SEM). The EDAX software is able to identify the relative concentrations of each of the alloying elements in the Usibor® 1500 P sample, and, as such, is able to map and measure the diffusion of aluminum, silicon, and iron within the surface

coating. Three measurements were made, one in the "hot" zone (in contact with the RA330®), one in the "cold" zone (in contact with the RSLE 57®), and one in the transition zone.

The concentrations of each of the primary constituents in each zone can be observed in Figure 40. The location where the surface coating ends, and the 22MnB5 substrate begins is marked by the steep drop in Al and Si, and a commensurate rise in Fe; this location effectively marks the extent of the coating thickness. It is easily observed that the coating thickness in the cold zone is 10 and 15 microns thinner than that in the hot and transition regions, respectively. This logically follows from the fact that the lower temperature of the cold zone results in less diffusion and growth of the Al, Si, and Fe via diffusive transport and Arrhenius rate kinetics. This is also supported by the substantially higher relative concentration of Al than the transitional and hot zones: without sufficient time and temperature, the Fe is unable to diffuse into the Al-Si coating.

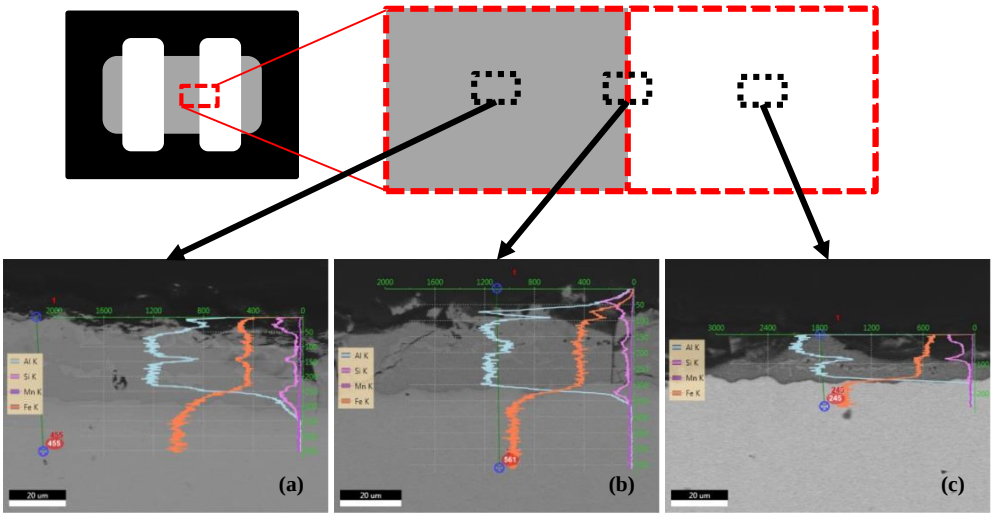

Figure 40 - EDS measurements of the (a) cold zone, (b) transition zone, and (c) hot zone in the 180 s sample at 1000x magnification.

Chapter 7
Conclusions and Future Work

From the results presented and discussed in Chapter 5 and Chapter 6, this final chapter summarizes the major conclusions of this work, and presents several recommendations for future research activities.

7.1 Conclusions

There is enormous pressure to improve process efficiency and part quality achieved through hot forming die quenching. While almost every industrial HFDQ line uses roller hearth or batch furnaces to austenitize coupons, this work demonstrates that a lab-scale direct contact heating apparatus can fully austenitize Usibor® 1500P blanks using less time, energy, and floor space compared to furnaces.

Tests were performed on a direct contact heating monolith constructed from a high nickel alloy, RA330, and was surrounded by high-temperature ceramic insulation to minimize heat loss. Twelve SiC elements with a net power output of 10 kW were used to heat the monolith, and maintain its operating temperature around 1000 °C. Usibor® 1500P steel coupons measuring 200 mm by 100 mm by 2 mm were used in all experiments; many of the coupons used were instrumented with K-type thermocouples in order to monitor their heating rate.

1D modelling predicted that the coupons being tested would reach the desired temperature of 950 °C in under 20 s; testing showed that direct contact heating required around 21 s of heating time to obtain full austenitization. Despite the rapid heating rate, complete austenitization was verified by dilatometric measurements performed in the Gleeble®. Compared with furnace treated samples, direct contact heated samples displayed comparable tensile strength, hardness, and microstructure. Additionally, this technology was shown to be capable of transforming the Al-Si coating into a permanent Al-Si-Fe intermetallic layer, complete with the intermetallic compounds typically found in furnace treated samples.

A potential drawback of direct contact heating concerns the adhesion of the molten Al-Si coating to the striking surface, which complicates blank transfer out of the heating monolith.

Testing of potential surface coatings suggested that a Metco®/Amdry® combined coating striking surface greatly reduced adhesion, and maintained a high-quality surface finish.

Finally, this work presents a novel direct contact heating method for rapidly tailoring mechanical properties of Usibor® 1500P coupons. The tailoring surface was constructed from RA330® with inlayed RSLE 57® insulation strips, resulting in drastically different coupon heating rates. 3D modelling showed that heating times would be greater than the homogeneous heating case, as axial conduction effects needed to be reconciled. It was found that the material hardness could be varied by up to 370 HV over a span as short as 6 mm. A comparison of hardness values from coupons heated from 20 to 180 s showed that longer heating times were necessary at this scale to fully austenitize the region in contact with the RA330®.

7.2 Future Work

7.2.1 Upscaling

While the results of this research supports the potential for success of direct contact heating in HFDQ, full upscaling, validation, and implementation in an industrial facility is still at least two to four years away. Because of the low-throughput nature of the lab-scale apparatus, it is unknown how the direct contact heated monolith will handle the high-throughput required of an industrial setting; concerns involving reheat time, heat loss due to increased surface area, and material and element resilience over long term use must be addressed. A long-term usability study would be required to verify that the use of the Amdry®/Metco® anti-adhesion surface treatment would be viable in an industrial setting. Additionally, as the types of steel that are used in HFDQ applications are improved and changed to utilize different coatings and required heat treatment regimes, it will eventually be necessary to test this heating methodology with alternative materials.

Presently, work is underway to construct a half-scale industrial prototype to test the scalability of the direct contact heating technology proposed in this work. This study will allow for a longer-term investigation into the feasibility of using this technology in an industrial setting. A more in-depth and higher-throughput surface fouling study should be done to ensure long-term usability. Additionally, in-die forming and quenching will be coupled with the

heating process on a single press. This will allow for a better comparison of the performance of components typically made by traditional HFDQ lines. Recent work by Ploshikhin et al. shows the use of a combined direct contact heating and radiative heating approach to enhance the development of the surface coating over the temperature range in which the Al-Si coating liquefies [50]. This approach could be tested in the half-scale prototype currently under development, albeit the heat treatment time would increase by several minutes.

Additionally, a more robust and reliable transfer mechanism has been developed and constructed by four undergraduate mechanical engineering students for their ME 481/482 Capstone Design Project. This mechanism will greatly improve the repeatability and operator safety of this upscaled process, as it is able to move hot blanks from the heated monolith to a forming/quenching die without any human interaction.

7.2.2 Tailoring

Building on the studies conducted and presented in this work, a large-scale tailoring plate will be constructed. With these experiments, the axial conduction effects observed in the lab-scale tests will be investigated. This will likely be done by reducing the ratio of the "hot" zone to the "cold" zone of the striking surface. A larger hot zone within the coupons would have relatively more thermal mass than the cold zones compared to the design presented in this thesis; this would allow the hot zone to be austenitized in less time (closer to that of the homogeneous heating regime), as the blank would have more internal energy to spare while not realizing as steep of a temperature gradient. This would allow for both a quickly austenitized region, as well as a gradient of mechanical properties.

7.2.3 Modelling

Further modelling work should be completed to analyze the thermal distribution in the upscaled die, as any thermal gradients would have a more pronounced effect on the final mechanical properties on a larger scale. Additionally, a Johnson-Mehl-Avrami-Kolmogorov (JMAK) type molecular kinetics model, often used to infer crystallization mechanisms [58], should be built

to more accurately predict the development of the Al-Si-Fe surface coating in the various zones of the tailoring die.

Appendix A
Semi-Infinite Slab Mathematical Treatment

Given the partial differential equation governing heat transfer within the Usibor® blank [35]:

$$\alpha \frac{\partial^2 T}{\partial x^2} - \frac{\partial T}{\partial t} = 0 \tag{12}$$

Because we are looking to design the monolith with a prescribed surface temperature T_s, we assume that the uniform initial condition is $T = T(x, t = 0) = T(t = 0)$, and therefore, the bounding surface and initial conditions are [35]:

$$\begin{aligned} &T(x = 0, t) = T_s \\ &T(x \to \infty, t) = T(t = 0) \\ &T(x, t = 0) = T(t = 0) \end{aligned} \tag{13}$$

It is noted that x and t have a semi-infinite range, such that $0 \le x, t \le \infty$ [35]. This, alongside the characteristics of the second-order PDE (1), allows us to define a similarity variable η that combines x and t, and enables the reduction of (1) to an ODE. This dimensionless similarity variable is defined as [35]:

$$\eta = \frac{x}{2(\alpha t)^{1/2}} \tag{14}$$

With a dimensionless similarity variable, it is also convenient to make temperature dimensionless by scaling with $T_s - T(t = 0)$ [35]. As such, we define dimensionless temperature, T^*, as [35]:

$$T^*(\eta) = \frac{T - T(t_0)}{T_s - T(t_0)}, 0 \le T^* \le 1 \tag{15}$$

Similarly, we are able to utilize η to reduce three boundary and initial conditions down to two; they are given as [35]:

$$\begin{aligned} &T^*(\eta = 0) = 1 \\ &T^*(\eta \to \infty) = 0 \end{aligned} \tag{16}$$

Therefore, by substituting in the dimensionless similarity variable and non-dimensional temperature into the original governing partial differential equation, we elicit an ordinary differential equation that is the dimensionless energy equation, given by [35]:

$$\frac{d^2T*}{d\eta^2} + 2\eta\frac{dT*}{d\eta} = 0 \tag{17}$$

The solution to (17) subject to the initial and boundary conditions given in (16) is [35]:

$$T* = \frac{T - T(t_0)}{T_s - T(t_0)} = 1 - \text{erf}(\eta) \tag{18}$$

Substituting for η, the temperature distribution in terms of x and t is given by [35]:

$$T(x,t) = T(t_0) + \left[T_s - T(t_0)\right]\left\{1 - erf\left[\frac{x}{2(\alpha t)^{1/2}}\right]\right\} \tag{19}$$

And, by differentiating (2), applying the chain rule, and evaluating the resultant at $x = 0$, the transient surface heat flux is found to be [35]:

$$\begin{aligned} q_{\rho c_p k}(t) = q_s(t) &= -k\left[T_s - T(t=0)\right]\left.\frac{\partial T*}{\partial x}\right|_{x=0} \\ &= -k\left[T_s - T(t_0)\right] = -\frac{k}{(\pi\alpha t)^{1/2}}\left[T_s - T(t_0)\right]\frac{\partial\eta}{\partial x}\frac{\partial T*}{\partial\eta} \\ &= -\frac{(\rho c_p k)^{1/2}}{\pi^{1/2}t^{1/2}}\left[T_s - T(t_0)\right] \end{aligned} \tag{20}$$

Appendix B

Heating Element Power Requirement Calculations

Recalling the need for a net output power of 10 kW to overcome any losses, and to overcompensate for error, it can be shown that

$$\frac{10,000W}{12elements} = 833.33\frac{W}{element} \tag{21}$$

$$\text{Watt Density} = \frac{W/element}{A/element} = \frac{833.33W}{151.6cm^2} = 5.5\frac{W}{cm^2} \tag{22}$$

$$E = \sqrt{WR} = \sqrt{(833.33W)(1.57\Omega)} = 36.2\frac{V}{element} \tag{23}$$

$$I = \frac{E}{R} = \frac{36.2V}{1.57\Omega} = 23.04A \pm 20\% \tag{24}$$

With the necessary power density calculated in Eq. (22), it was confirmed by the manufacturer that a sufficient heat load should be generated, assuming the voltage and current calculated in Equations (23) and (24) could be supplied in the lab. Fortunately, the High Pressure Lab had two 220 V, 30 A circuits available, thus ensuring sufficient power output was possible for the heating elements.

Bibliography

[1] A. Hund, "Continuous Improvement of Hot Forming Technology," in *3rd International Conference on Sheet Metal Forming of High Performance Steel*, Kassel, Germany, 2011.

[2] B. A. Behrens, F. W. Bach, M. Diekamp, S. Hübner, F. Nürnberger, J. Schrödter, L. Wolf and J. Moritz, "Process Time Reduction of Hot Stamping by Means of Early Extraction from the Press," in *4th International Conference on Hot Sheet Metal Forming of High-Performance Steel*, Luleå, Sweden, 2013.

[3] A. Ingebrand, I. V. Anglès and T. Laumann, "Integrated and Competitive Tooling Solutions for the Production of Tailored Components and Cutting of UHSS," in *3rd International Conference on Hot Sheet Metal Forming of High Performance Steel*, Luleå, Sweden, 2011.

[4] G. B. G. Gucker, "From Profile Hardening to Custom Made Components," in *1st International Conference on Hot Sheet Metal Forming of High-Performance Steel*, Kassel, Germany, 2008.

[5] F.-J. Lenze, L. Banik and S. Sikora, "Applications of Hot Formed Parts for Body in White," in *IDDRG Conference*, Olofström, Sweden, 2008.

[6] R. Kolleck, R. Veit, H. Hofmann and F.-J. Lenze, "Alternative Heating Concepts for Hot Sheet Metal Forming," in *1st International Conference on Hot Sheet Metal Forming of High-Performance Steel*, Kassel, Germany, 2008.

[7] K. Steinhoff, N. Saba, M. Maikraz-Valentin and U. Weidig, "Optimized Process and Products in Hot Sheet Metal Forming," in *2nd International Conference on Hot Sheet Metal Forming of High Performance Steel*, Luleå, Sweden, 2009.

[8] A. Bardelcik, High Strain Rate Behaviour of Hot Formed Boron Steel with Tailored Properties, Waterloo: University of Waterloo, 2012.

[9] M. G. Twynstra, K. J. C. E. Daun, N. Adam and D. Womack, "Modeling and Optimization of a Batch Furnace for Hot Stamping," in *ASME Summer Heat Transfer Conference*, Minneapolis, MN, 2013.

[10] H. Lehmann, "Developments in the Field of Schwarz Heat Treatment Furnaces for Press Hardening Industry," in *3rd International Conference on Hot Sheet Metal Forming of High Performance Steel*, Kassel, Germany, 2011.

[11] R. George, A. Bardelcik and M. J. Worswick, "Hot Forming of a Lab-Scale B-Pillar with Tailored Properties–Experiment and Modelling," in *3rd International Conference on Hot Sheet Metal Forming of High-Performance Steels*, Kassel, 2011.

[12] M. Merklein and J. Lechler, "Investigation of the thermo-mechanical properties of hot stamping steels," *Journal of Materials Processing Technology*, pp. 452-455, July 2006.

[13] A. Bardelcik, C. P. Salisbury, S. Winkler, M. A. Wells and M. J. Worswick, "Effect of Cooling Rate on the High Strain Rate Properties of Boron Steel," *International Journal of Impact Engineering*, vol. 6, no. 37, pp. 694-702, 2010.

[14] J. Wilsius, B. Tavernier and D. Abou-Khalil, "Experimental and numberical investigation of various hot stamped B-pillar concepts based on Usibor® 1500P," in *3rd International Conference on Hot Sheet Metal Forming of High-Performance Steel*, Kassel, 2011.

[15] T. Stöhr, J. Lechler and M. Merklein, "Investigations on different strategies for influencing the microstructural properties with respect to partial hot stamping," in *2nd International Conference on Hot Sheet Metal Forming of High Performance Steel*, Luleå, 2009.

[16] O. Akisue and T. Hada, "Past Development and Future Outlooks of Automotive Sheet Steels," Nippon Steel, 1995.

[17] A. P. Krupitzer, "Steel is up to the AUTOMOTIVE CHALLENGE," 5 April 2012. [Online]. Available: http://machinedesign.com/metals/steel-automotive-challenge. [Accessed 8 June 2015].

[18] H. Karbasian and A. Tekkaya, "A Review on Hot Stamping," *Journal of Materials Processing Tecnology*, pp. 2103-2118, 19 07 2010.

[19] W. J. Joost, "Reducing vehicle weight and improving US energy efficiency using integrated computational materials engineering," *Jom*, vol. 64, no. 9, pp. 1032-1038, 2012.

[20] ArcelorMittal, “Steels for Hot Stamping,” 19 01 2012. [Online]. Available: http://www.arcelormittal.com/automotive/saturnus/sheets/catalogue.pl?id_sheet=E&header=&language=EN.

[21] S. S. Babu, G. M. Goodwin, R. J. Rhode and B. Sielen, "Effect of Boron on the Microstructure of Low-Carbon Steel Resistance Seam Welds," *Welding Journal*, vol. 1, no. 77, pp. 249-253, 1998.

[22] Bricmont, "Roller Hearth Furnace," 2012. [Online]. Available: http://www.bricmont.com/RollerHearth.aspx. [Accessed 07 10 2012].

[23] Thermo Transfer Inc., "Roller Hearth Furnaces," 2012. [Online]. Available: http://thermotransferinc.com/index.php/roller-hearth-furnaces/. [Accessed 07 10 2012].

[24] K. Mori, S. Maki and Y. Tanaka, “Warm and hot stamping of ultra tensile strength steel sheets using resistance heating,” *CIRP Annals - Manufacturing Technology*, vol. 54, no. 1, pp. 209-212, 2009.

[25] T. Maeno, K.-i. Mori, M. Sakagami and Y. Nakao, "Full Hardening of Products in Hot Spamping Using Rapid Resistance Heating," in *5th International Conference on Hot Sheet Metal Forming of High Performance Steel*, Toronto, 2015.

[26] R. Kolleck, R. Veit, M. Merklein, J. Lechler and M. Geiger, “Investigation on Induction Heating for Hot Stamping of Boron Steels,” *CIRP Annals - Manufacturing Technology*, vol. 58, pp. 275-278, 2009.

[27] L. Larsson, *Warm Sheet Metal Forming with Localized In-Tool Induction Heating*, Lund University, 2005.

[28] R. E. Haimbaugh, Practical Induction Heat Treating, Materials Park, Ohio: ASM International, 2001, pp. 5-18.

[29] V. Ploshikhin, A. Prihodovsky, J. Kaiser, R. Bisping, H. Linder, C. Lengsdorf and K. Roll, "New Heating Technology for Furnace-Free Press Hardening Process," in *Tools and Technologies for Processing Ultra-Heigh Strength Materials*, Graz, Austria, 2011.

[30] F. Zimmermann, J. Spörer and W. Volk, "Partial Tempering of Press Hardened Steels by Firect Flame Impingement - the Review of an Alternative Approach for Tailored Properties," in *5th International Conference on Hot Sheet Metal Forming of High Performance Steel*, Toronto, 2015.

[31] K. Omer, A. Bardelcik, R. George, M. Worswick, D. Detwiler, S. Malcolm and N. Adam, "Development and Testing of a Hot Stamped Axial Crush Member with Tailored Properties," in *5th International Conference on Hot Sheet Metal Forming of High Performance Steel*, Tornto, 2015.

[32] B.-A. Behrens, H. J. Maier, F. Nürnberger, J. Schrödter, J. Moritz, L. Wolf and C. M. Gaebel, "Hot Forming and Subsequent Cooling Outside the Press for Adjusted Tailored Properties of 22MnB5 Steel Sheets," in *5th International Conference on Hot Sheet Metal Forming of High Performance Steel*, Toronto, 2015.

[33] M. Schaefer, D. Schuoecker, J. Aichinger, O. Spitzer and T. Harrer, "Laster Softening of Press Hardened Steel in High Volume Laser Production Lines," in *5th International Conference on Hot Sheet Metal Forming of High Performance Steel*, Toronto, 2015.

[34] H. Lehmann, "New Developments in Furnace for Press-Hardening," in *5th International Conference on Hot Sheet Metal Forming of High Performance Steel*, Toronto, 2015.

[35] M. Kaviany, Principles of Heat Transfer, New York: John Wiley & Sons, 2002.

[36] T. L. Bergman, A. S. Lavine, F. P. Incropera and D. P. Dewitt, Fundamentals of heat and mass transfer, John Wiley & Sons, 2011.

[37] J. R. Howell, R. Siegel and M. P. Mengüç, Thermal Radiation Heat Transfer, Boca Raton: CRC Press, 2011.

[38] J. R. Lloyd and W. R. Moran, "Natural convection adjacent to horizontal surface of various planforms," *Journal of Heat Transfer*, vol. 4, no. 96, pp. 443-447, 1974.

[39] Rolled Alloys, “RA330 Data Sheet,” 2011. [Online]. Available: http://content.rolledalloys.com/technical-resources/databooks/RA330_DB_US_EN.pdf.

[40] E. J. F. R. Caron, K. J. Daun and M. A. Wells, "Experimental Heat Transfer Coefficient Measurements during Hot Forming Die Quenching of Boron Steel at High Temperatures," *International Journal of Heat and Mass Transfer,* vol. 71, pp. 396-404, 2014.

[41] M. Nadri, A. Saeed-Akbari and W. Bleck, "The Effects of Non-isothermal Deformation on Maternsitic Transformation in 22MnB5 Steel," *Materials Science and Engineering A,* vol. 487, pp. 445-455, 2008.

[42] R. Gregorieva, "Study of Phase Transformations in Al-Si Coating During the Austenitization Step," *Solid State Phenomena,* Vols. 172-174, pp. 784-790, 2011.

[43] I Squared R Element Co., "Type SE and TSE, Silicon Carbide Spiral Heating Elements," [Online]. Available: http://www.isquaredrelement.com/pdf/se-lettersize.pdf. [Accessed 05 12 2012].

[44] Aremco, "High Temperature Ceramic-Metallic Pastes," Aremco, 2015. [Online]. Available: http://www.aremco.com/ceramic-metallic-pastes/. [Accessed 2015].

[45] A. Bardelcik, M. J. Worswick, S. Winkler and M. A. Wells, "A strain rate sensitive constitutive model for quenched boron steel with tailored properties," *International Journal of Impact Engineering,* no. 50, pp. 49-62, 2012.

[46] OMEGA Engineering Inc., "Temperature, Process and Strain Controllers," [Online]. Available: http://www.omega.com/temperature/pdf/CNI_SERIES.pdf. [Accessed 13 July 2015].

[47] R. George, "Hot Forming of Boron Steels with Tailored Mechanical Properties," Waterloo, 2011.

[48] "ASTM Standard E8/E8M 2013a, Standard Test Methods for Tension Testing of Metallic Materials," ASTM International, West Coshohocken, PA, 2013.

[49] B. Pawłowski, "Dilatometric examination of continuously heated austenite formation in hypoeutectoid steels," *Journal of Achievements in Materials and Manufacturing Engineering*, vol. 54, no. 2, pp. 185-193, 2012.

[50] V. Ploshikhin, A. Prihodovsky, J. Kaiser and L. Skutella, "Contact heating - New heating technology for heat treatment and hot forming," in *Tools and Technologies for Processing Ultra High Strength Materials*, Graz, 2013.

[51] M. Nadiri, A. Saeed-Akbari and W. Bleck, "The Effects of Non-isothermal Deformation on Maternsitic Transformation in 22MnB5 Steel," *Materials Science and Engineering A*, vol. 487, pp. 445-455, 2008.

[52] L. Garcia Aranda, Y. Chastel, J. Fernández Pascual and T. Dal Negro, "Experiments and simulation of hot stamping of quenchable steels," *Adv Technol Plast*, no. 2, pp. 1135-1140, 2002.

[53] W. J. Cheng and C. J. Wang, "Effect of silicon on the formation of intermetallic phases in aluminide coating on mild steel," *Intermetallics*, vol. 19, no. 10, pp. 1455-1460, 2011.

[54] M. Windmann, A. Röttger and W. Theisen, "Phase formation at the interface between a boron alloyed steel substrate and an Al-rich coating," *Surface and Coatings Technology*, no. 226, pp. 130-139, 2013.

[55] T. Maitra and S. P. Gupta, "Intermetallic compound formation in Fe–Al–Si ternary system: Part II," *Materials Characterization*, vol. 49, pp. 293-311, 2003.

[56] Z.-X. Gui, K. Wang, Y.-S. Zhang and B. Zhu, "Cracking and interfacial debonding of the Al-Si coating in hot stamping of pre-coated boron steel," *Applied Surface Science*, no. 316, pp. 595-603, 2014.

[57] Zircar Refractory Composites Inc., "Refractory Board Types," [Online]. Available: http://www.zrci.com/zircal95.htm. [Accessed 13 October 2012].

[58] M. C. Weinberg, D. P. Birnie and V. A. Shneidman, "Crystallization kinetics and the JMAK equation," *Journal of Non-Crystalline Solids*, no. 219, pp. 89-99, 1997.

[59] ASTM Standard E8/E8M-09, West Conshohocken, PA, DOI: 10.1520/E0008_E0008M-09, www.astm.org: ASTM International.

[60] K. Mori, S. Maki and Y. Tanaka, "Tailored Die Quenching of Steel Parts Having Strength," *Journal of Materials Processing Technology*, vol. 213, pp. 508-514, 2013.

[61] M. Meyers and K. Chawla, Mechanical Behaviours of Materials, New York: Cambridge University Press, 2009, p. 347.

[62] "ASTM Standard 1033-10, Standard Practice for Quantitative Measurement and Reporting of Hypoeutectoid Carbon and Low-Alloy Steel Phase Transformations," ASTM International, West Conshohocken PA, 2010.

[63] J. Brecht, S. Pohl, A. Schlender and H. Voswinckel, "Hotformed Tailor Rolled Products, Tailored Light-weight Design Solutions for the Vehicle Structure," in *5th International Conference on Hot Sheet Metal Forming of High Performance Steel*, Toronto, 2015.